UNIVERSIDADE DE LISBOA
FACULDADE DE CIÊNCIAS
DEPARTAMENTO DE FÍSICA

Dynamics of active particles in the presence of obstacles

Vasco Correia Braz

Mestrado em Física
Especialização em Física Estatística e Não Linear

Dissertação orientada por:
Prof. Dr. Nuno Araújo

2019

Acknowledgements

I start to acknowledge the shared experimental work of Dr.Giorgio Volpe, Dr. Stanislaw Makarchuk and Dr. Lena Ciric from the University College of London. Their results are the inspiration for the models proposed and reported here.

I thank all the CFTC members for the fruitful discussions about active matter and statitical physics.

I would like to thank specially to my supervisor Nuno Araújo, for the opportunity he gave me to work on such an interesting topic, for his guidance, and the confidence he gave me to tackle new physical problems.

Lastly I would also like to particularly thank André Nunes, who helped me in my first attempts to work with Brownian Dynamics, and to my office mates, Pedro Neta, Francisco Cerdeira and Gonçalo Paulo, not only for the constant supply of pens and papers, but mainly for the friendship and support they provided.

Abstract

Bacteria are among the simplest organisms that have the capability to metabolize nutrients from their environment and converting them into directed motion. This self-propulsion is what allows them to explore the environment in a very efficient way and to avoid toxic compounds. A deeper understanding of their collective dynamics and of the constraints to an efficient mobility is pivotal to solve open problems, such as, the spread of bacterial diseases in the human body or cell proliferation. The possibility of designing new micro-materials, inspired by these biological agents, might also be of a relevant technological impact in different contexts, such as cleaning of oceans or in the development of non-invasive medical treatments. When moving near a substrate some bacteria exhibit chiral trajectories moving in circular like paths. In this work, we aim at studying the motion of such chiral active particles in complex environments, in particular, to help to elucidate the results obtained experimentally by the group of Dr. Giorgio Volpe at the University College of London, showing how the individual and collective dynamics of bacteria ($E.coli$) are strongly influenced by the presence of physical obstacles. The main results show that the overall mobility of bacteria is in fact enhanced for an optimal concentration of obstacles. The main results of this thesis have been published in Nature Communications [10, 4110 (2019)].

Keywords: Active matter systems, complex environments, chiral particles.

Resumo

As bactérias são um dos muitos tipos de organismos que têm a capacidade de metabolizar compostos do ambiente externo para executar movimento direcionado. Este mecanismo de autopropulsão permite-lhes explorar o ambiente de uma forma muito eficiente e evitar compostos tóxicos. Ao entender a sua dinâmica colectiva e quais podem ser as restrições para uma mobilidade eficiente, estamos mais preparados para lidar com problemas como a disseminação de doenças bacterianas no corpo humano ou proliferação celular, mas também para desenhar novos micro-materiais com potenciais aplicações em diferentes contextos, como limpeza de oceanos.

Matéria capaz de extrair energia do exterior e converte-la em energia cinética como de bactérias e células é designada como matéria activa. Quando em solução, dadas as suas dimensões, o seu movimento é afetado por flutuações térmicas, tal como acontece com as partículas passivas. No entanto, o fluxo de energia que resulta em movimento direcionado faz com que estes sistemas estejam fora do equilíbrio termodinâmico, colocando vários desafios ao seu estudo teórico. Este tipo de organismos (ou objectos artificiais) vivem (ou pretende-se que actuem) em ambientes complexos sendo de esperar que a sua dinâmica seja altamente influenciada por constrangimentos físicos, composição química e heterogeneidade do meio. Observa-se por exemplo que algumas partículas efectuam um movimento quiral quando confinadas a duas dimensões.

Neste trabalho pretendemos estudar o movimento de bactérias em ambientes complexos, em particular compreender do ponto de vista teórico os resultados preliminares obtidos experimentalmente pelo grupo do Dr. Giorgio Volpe na University College de Londres. Estes resultados sugerem que a dinâmica individual e coletiva de bactérias ($E.coli$) é fortemente influenciada pela presença de obstáculos físicos. Um dos resultados principais mostra que a mobilidade geral das bactérias é de facto aumentada para uma concentração intermédia de obstáculos. Apresentamos um modelo numérico que reproduz o comportamento observado e que é capaz de identificar qual o mecanismo responsável pelo aumento de mobilidade para uma densidade óptima de obstáculos. Fazemos um estudo sistemático dos parâmetros que o compõe, com objectivo de perceber de que forma os diferentes constrangimentos físicos, estejam eles associados ao meio envolvente ou aos próprios elementos activos, influenciam o comportamento e em particular a mobilidade de matéria activa em ambientes complexos.

Palavras-chave: Sistemas de matéria activa, ambientes complexos, movimento quiral.

Contents

List of Figures

Chapter 1

Introduction

Since the pioneer work of Einstein [10] and Perrin [28], the study of Brownian particles has attracted significant research effort. By relating elementary microscopic phenomena to macroscopic observable quantities, several fundamental developments have been achieved in equilibrium and non-equilibrium statistical physics [4, 18]. The subject of Brownian motion has also made an impact in several fields outside the realms of physics such has in mathematics, namely in the development of stochastical diferential equation and probability theory [16, 14] or economy [5]. Recently, the interest has shifted towards active particles which are able to extract energy from their surroundings and convert it into directed motion [32, 1]. In this class of systems, the stimuli that govern their individual and collective behaviors are not only external, as in the case of passive Brownian particles, but originate from the elements themselves as in the case of several biological systems such has a colony of cells, where each individual is able to move and grow using the internal energy that they have accumulated by consuming nutrients. Many more examples exist in nature and can be found at different scales, such as, bacteria or cells, like the *E.coli* [21, 2] and spermatozoa [11], birds and fishes whose collective dynamics gives rise to complex swarms [36] or even molecular motors. However, even though most examples of self-propelled active matter are living systems, there has been in the last few years a sustained interest in artificial active systems such as synthetic micro-robots [29, 27] or driven granular matter (as the vibrated polar disks in [8]). One of the most studied examples are the so-called active Janus particles. These are typically spherical particles composed of different materials at the surface of each of its hemispheres and that, by reacting with the surrounding fluid in an asymmetric way, are able to convert chemical energy into kinetic energy in the form of a self-propulsion [31, 11].

Many applications arise from the study of these systems. Understanding the formation of biofilms may allow us to find new ways to treat or even prevent bacterial infections [15]. The fabrication of micro or nanoswimmers might help the realization of several non-invasive medical tasks such as targeted drug delivery, material removal, or diagnosis by telemetry [26]. Another possibility is the application of artificial swimmers to the cleaning of oceans and quality control of the environment [13]. From a more fundamental point of view, it is also important to notice the interest and relevance of this topic in the general framework of condensed matter and statistical physics. The existence of a constant flow of energy drives these systems far from equilibrium, what requires new theoretical tools, different from the usual ones that typically assume the existence of thermodynamic equilibrium. Interestingly, systems composed of active self-propelled particles are also fundamentally different from the others out-of-equilibrium systems. Ramaswamy [32] highlights two of the main features of these systems that distinguishes them from other types of non-equilibrium systems:

(a)“The energy input takes place directly at the scale of each active particle and is thus homoge-

neously distributed through the bulk of the system, unlike sheared fluids or three-dimensional bulk granular matter, where the forcing is applied at the boundaries";

(b) "The direction of self-propelled motion is set by the orientation of the particle itself, not fixed by an external field."

Nevertheless, while it is important to understand the motion and specific mechanisms of each of these micro-swimmers, to fully understand, and be able to perform the applications mentioned above, it is important to also consider the role of the surrounding medium. For example, confinement may alter the typical behavior of micro-swimmers. It has been known for a long time now, that some flagellated bacteria alter their typical trajectories when moving near a surface, exhibiting circular like motion whose shape looks like spirals interchanged with random changes of directions i.e, chiral motion [17]. There have been many recent studies [40, 34, 33, 37] showing how the complexity or randomness of the environment influences the individual and collective behavior of active elements. In particular, it was shown experimentally [25] that a random distribution of obstacles in two-dimensional set up of active colloids hinders their mobility.

In the context of an ongoing collaboration with the group where this thesis was developed, it was recently shown experimentally by Giorgio Volpe, Stanislaw Markachuk and Lena Ciric, from the University College of London, that when swimming in a environment with a relatively low density of micron sized obstacles, chiral flagellated bacteria see their mobility enhanced for an optimal concentration of obstacles.

The purpose of this work is to explain the underlying mechanism responsible for the enhancement observed in the proliferation of chiral bacteria in an environment with a low density of obstacles. We employ Brownian Dynamics to simulate the trajectories of active chiral particles in an heterogeneous environment of immobile obstacles. We develop a numerical model where an extra interaction between bacteria and obstacles (besides pure repulsion) is proposed. We argue that this (forward-scattering) interaction is responsible for the increase in the mobility of these agents. We parameterize our model according to the experimental data. To further explore our model, we perform a systematic study in the space of the parameters used.

In Chapter 2, we make a brief review about Brownian motion to set the basis for modeling active particles. We introduce the Langevin approach and how to use it to model micro-swimmers in a homogeneous solution and from that deduce some fundamental relations. In Chapter 3, we introduce the concept of chiral active motion. We describe the recent experiments that motivate this work, we extend the Langevin approach to chiral active matter and present our model and the results obtained with it. In Chapter 4, we explore the space of parameters of our model and identify what are the fundamental relations that should be considered to predict the behavior of the system in different physical conditions. In chapter 5, we check if our system verifies invariant properties of active random walks shown in previous works and under what conditions that happens. Finally, in chapter 6 we draw some conclusions.

Chapter 2

Langevin approach: from passive to active systems

Most of the particle-based models used to describe the behavior of micro-organisms and small animals are based on Brownian motion. This phenomenon got its name from the Scottish botanist Robert Brown. Brown observed that pollen grains in a fluid perform an erratic motion that is not caused by the grains itself but by some interaction with the surrounding fluid. The first theoretical works on the subject were by Einstein in 1905 [10], Smolukowski in 1906 [38], and Langevin in 1908 [23]. Using different approaches, the three physicists showed that the responsible for this "random" motion is the thermal fluctuations in the velocity of the molecules of the surrounding fluid.

Einstein's approach starts from the hypothesis that kinetic energy of the fluid is responsible for the grains motion and he deduces from that a differential equation to describe the time evolution of the probability density function of a Brownian particle. From this, he was able to derive an expression for the mean squared displacement (MSD), a measure of how a particle departs on average from an initial reference point. Paul Langevin introduced a "complementary force" applied by the fluid molecules that affects the velocity of the Brownian particle and that keeps them moving where they would eventually stop due to the friction of the fluid. Since the Langevin approach implies a stochastic differential equation (a stochastic version of Newton's second law) to be applied for each Brownian particle, it is a much more useful technique to use and where to include new microscopic mechanisms and constraints such as the activity of the particle (self-propulsion) or possible irregularities in the environment and for numerical approaches.

2.1 Passive Brownian motion

The Langevin approach for a Brownian particle in a fluid is a phenomenological way to treat these particles, assuming that they move due to the collisions with the molecules present in the surrounding fluid. The interaction with the fluid is written as a superposition of a random force, described by a stochastic random variable $\vec{\xi}$, and a drag term that describes the resistance offered by the fluid to the particle's motion when this moves against it. This resistance is modeled using a term proportional to the velocity of the Brownian particle. The Langevin equation of motion is then a stochastic version of Newton's second law:

$$m\frac{d\vec{v}}{dt} = -\gamma\vec{v} + \vec{\xi}. \tag{2.1}$$

The first term on the right hand side is a dissipative term proportional to the particle's velocity where $\gamma = 6\pi\eta R$ corresponds to the Stokes coefficient of a sphere. The second term $\vec{\xi}(t)$ is the stochastic variable that accounts for the microscopic collisions between the particle and the fluid molecules and that accelerate the particle in random directions. There are some statistical properties that should be imposed on $\vec{\xi}(t)$:

(i) On average the total force felt at each instant is null since there is equal probability of suffering collisions from any side, $\langle\vec{\xi_i}(t)\rangle = 0$;

(ii) For the timescale of relevance, we may assume the the stochastic variables are independent in time and space and so we assume a second moment give by $\langle\vec{\xi_i}(t)\vec{\xi_i}(t)\rangle = \Gamma\delta_{ij}\delta(t-t')$. Γ is a constant that sets the intensity of the force.

The solution of Eq. (2.1) can be obtained by first finding the solution for the homogeneous equation.

This solution gives the velocity of the particle at each instant (influenced only by the drag term). Assuming as initial condition $v(t = 0) = \vec{v_0}$, we have the expression :

$$\vec{v}(t) = \vec{v_0}e^{-\frac{\gamma}{m}t}. \tag{2.2}$$

To find the particular solution we solve Eq. (2.1), by choosing the integrating factor $e^{\frac{\gamma t}{m}}$, and the general solution is then

$$\vec{v}(t) = \vec{v_0}e^{-\frac{\gamma}{m}t} + e^{-\frac{\gamma t}{m}}\int_0^t e^{\frac{\gamma t'}{m}}\frac{\vec{\xi(t')}}{m}dt'. \tag{2.3}$$

Since $\langle\vec{\xi(t)}\rangle = 0$ the average value of $\vec{v}(t)$ is $\langle\vec{v(t)}\rangle = \vec{v_0}e^{-\frac{\gamma}{m}t}$. The second moment is

$$\begin{aligned}
\langle v^2(t)\rangle &= \langle v_0^2 e^{-2\frac{\gamma t}{m}} + 2v_0^2 e^{-2\frac{\gamma}{m}t}\int_0^t e^{\frac{\gamma t'}{m}}\frac{\vec{\xi}(t')}{m}dt' + \\
&+\frac{e^{-2\frac{\gamma t}{m}}}{m^2}\int_0^t\int_0^t e^{\frac{\gamma}{m}(t'+t'')}\vec{\xi}(t')\vec{\xi}(t'')dt'dt''\rangle = \\
&= \langle v_0^2\rangle e^{-2\frac{\gamma t}{m}} + \frac{e^{-2\frac{\gamma t}{m}}}{m^2}\int_0^t\int_0^t e^{\frac{\gamma}{m}(t'+t'')}\langle\vec{\xi}(t')\vec{\xi}(t'')\rangle dt'dt'' = \\
&= \langle v_0^2\rangle e^{-2\frac{\gamma t}{m}} + \frac{e^{-2\frac{\gamma t}{m}}}{m^2}\int_0^t\int_0^t e^{\frac{\gamma}{m}(t'+t'')}\Gamma\delta_{ij}\delta(t'-t'')dt'dt'' = \\
&= \langle v_0^2\rangle e^{-2\frac{\gamma t}{m}} + \frac{e^{-2\frac{\gamma t}{m}}}{m^2}\int_0^t e^{\frac{\gamma}{m}(2t'')}\Gamma\delta_{ij}dt''.
\end{aligned} \tag{2.4}$$

Integrating the last term, we obtain

$$\langle\vec{v}^2(t)\rangle = v_0^2 e^{-2\frac{\gamma}{m}t} + \frac{d\Gamma}{2\gamma m}(1 - e^{-2\frac{\gamma}{m}t}). \tag{2.5}$$

In the asymptotic limit ($t \to \infty$), we assume that the particle is in thermodynamic equilibrium with the fluid, at thermostat temperature T, and so the equipartition theorem applies. Since the first term on the right hand side of Eq. (2.5) vanishes we obtain

$$\langle v^2(t \to \infty)\rangle = \frac{d\Gamma}{2\gamma m} = \frac{dk_B T}{m}, \tag{2.6}$$

and $\Gamma = 2\gamma k_B T$. From Eq. (2.3) we can also obtain the displacement of the particle from its initial position,

$$\vec{r}(t) - \vec{r}(0) = \int_0^t v_0 e^{-\frac{\gamma}{m}t} dt + \int_0^t \int_0^{t'} e^{-\frac{\gamma}{m}(t-t'')} \frac{\vec{\xi}(t'')}{m} dt'' dt'. \tag{2.7}$$

Finally, we can determine the mean squared displacement of a Brownian particle. This is a useful way to quantify the average displacement of particle by calculating the square of the deviation of the particle's position relative to some reference point (in this case $\vec{r}(t=0)$),

$$\mathrm{MSD}(t) = \langle (\vec{r}(t) - \vec{r}(0))^2 \rangle = \sum_{j=0}^{j=d} \langle (x_j(t) - x_j(0))^2 \rangle. \tag{2.8}$$

Where d corresponds to the spatial dimension. If we take $x_j(0) = 0$,

$$\begin{aligned} \langle (x_j(t) - x_j(0))^2 \rangle &= \frac{v_0^2 m^2}{\gamma^2}(1 - e^{-\frac{\gamma t}{m}})^2 \\ + \int_0^t dt_1 \int_0^t \langle \frac{\xi_j(t_1)\xi_j(t_2)}{\gamma^2} \rangle [1 - e^{-\gamma(t-t'')}][1 - e^{-\gamma(t-t')}] &= \\ = \frac{v_0^2 m^2}{\gamma^2}(1 - e^{-\frac{\gamma t}{m}})^2 + \frac{\Gamma}{\gamma^2 m} \int_0^t dt_2 [1 + e^{-2\gamma(t-t_2)} - 2e^{-\gamma(t-t_2)}] &= \\ = \frac{v_0^2 m^2}{\gamma^2}(1 - e^{-\frac{\gamma t}{m}})^2 + \frac{\Gamma}{\gamma^2}(t - 3\frac{m}{2\gamma} + \frac{2me^{-\frac{\gamma}{m}t}}{\gamma} - \frac{me^{-2\frac{\gamma}{m}t}}{2\gamma}) \end{aligned} \tag{2.9}$$

if the relaxation times τ_p are much shorter than the time scales of observation ($\tau_p << \Delta t$), we can consider that it always moves with terminal velocity thus ignoring any inertial terms. This is often a reasonable assumption, in this limit, the system is said to be in an overdamped regime where the relaxation time is negligible. In the overdamped regime,

$$\mathrm{MSD}(t) \sim 2d\frac{k_b T}{\gamma} t. \tag{2.10}$$

We have then the Stokes-Einstein relation that gives the characteristic diffusion coefficient of a given particle in a fluid, as $D_T = \frac{k_b T}{\gamma}$.

From the results deduced, one can see that a Brownian particle moves in a stochastic way but when averaging over an ensemble of such particles, we see that they depart from the initial position, not linearly with time (as it would for a ballistic kind of motion) but with relation that is proportional to the square root of t. Such behavior is called diffusive motion and it is characteristic of Brownian particles.

2.2 Active Brownian motion

The organisms that we want to study are able to self-propel in solution. However, since their sizes are typically of the order of microns, they are also subjected to thermal fluctuations. We can then think of a micro-swimmer as an active Brownian particle and consider an extra term to the Langevin equation Eq. (2.1) that accounts for the particle activity (i.e, the ability to self propel). For organisms that live in viscous solutions, where the viscous forces are much higher than their inertia, the typical relaxation times are very short and we may assume the overdamped regime ($\tau_p \to 0$). Bacteria, for example, have typical masses of the order of $m = 10^{-12}$ g [30] and, assuming a spherical shape with radius $R = 1$ μm,

a drag coefficient of about $\gamma = 10^{-9}$ kgs^{-1} (in water). For this kind of organisms, we have a typical relaxation time of about 10^{-6} s. A modified version of the Langevin equation in the overdamped regime for active particles is written in two dimensions as

$$\frac{dx(t)}{dt} = v\cos\theta(t) + \xi_x, \tag{2.11}$$

$$\frac{y(t)}{dt} = v\sin\theta(t) + \xi_y. \tag{2.12}$$

Here, the different spatial degrees of freedom are coupled by an angle θ that sets the direction of self-propulsion. Since this direction will also suffer from the interactions with the fluid molecules, performing its own diffusion, it will evolve in time according to:

$$\frac{d\theta(t)}{dt} = \xi_\theta. \tag{2.13}$$

The diffusion constant of rotation of a sphere is given by:

$$D_{\mathrm{R}} = \tau_{\mathrm{R}}^{-1} = \frac{k_{\mathrm{B}}T}{8\pi\eta R^3}. \tag{2.14}$$

Since $\theta(t)$ corresponds to the sum of many random variables over time, its value is expected to follow a probability density function that can be deduced from Wick's theorem as

$$P\Big(\theta(t)\Big) = \frac{1}{\sqrt{4\pi D_R t}} e^{\frac{-\theta^2}{4D_R t}}. \tag{2.15}$$

Having this into account, we can calculate the average trajectories of such Brownian agents. Assuming that at the initial time $t = 0$ we have $x(0) = 0$ and $y(0) = 0$,

$$\langle x(t)\rangle = v\int_0^t \langle\cos\theta\rangle dt \tag{2.16}$$

where

$$\langle\cos\theta\rangle = \int_{-\infty}^{+\infty} \cos\theta \frac{1}{\sqrt{4\pi D_R t}} e^{\frac{-\theta^2}{4D_R t}} d\theta. \tag{2.17}$$

This integral is solved using the result in the Appendix and choosing $\theta_0 = 0$ and $\alpha = 0$.

We can then write the integral [Eq. (2.16)] as

$$\langle x(t)\rangle = v\int_0^t e^{-D_R t} dt \tag{2.18}$$

Finally, by performing the above integral, and using the same procedure for $\langle y\rangle$ we obtain the average trajectory of a Brownian agent in a viscous fluid:

$$\langle x(t)\rangle = \frac{v}{D_{\mathrm{R}}}\left[1 - \exp\left(-D_{\mathrm{R}}t\right)\right] = v\tau_{\mathrm{R}}\left[1 - \exp\left(-\frac{t}{\tau_{\mathrm{R}}}\right)\right], \tag{2.19}$$

$$\langle y(t)\rangle = 0. \tag{2.20}$$

The above expression shows that the Brownian active particle will tend to move in an initial preferred direction (in this case $\theta_0 = 0$) for a typical time $\tau_R = \frac{1}{D_R}$, while it will on average stay stay in the position ($v\tau_R$,0) for longer times ($t >> \tau_R$).

MSD of an active Brownian agent

We now perform the calculation for the mean squared displacement of an active Brownian particle in 2 dimensions. To get the MSD, we need to solve the following integrals:

$$\begin{aligned}\left\langle (x(t)-x_0)^2 \right\rangle =& v^2 \int_0^t \mathrm{d}t_1 \int_0^t \mathrm{d}t_2 \left\langle \cos\theta\left(t_1\right)\cos\theta\left(t_2\right)\right\rangle \\ &+ \frac{2v}{\gamma}\int_0^t \mathrm{d}t_1 \int_0^t \mathrm{d}t_2 \left\langle \cos\theta\left(t_1\right)\xi_x\left(t_2\right)\right\rangle + \frac{1}{\gamma^2}\int_0^t \mathrm{d}t_1 \int_0^t \mathrm{d}t_2 \left\langle \xi_x\left(t_1\right)\xi_x(t_2)\right\rangle,\end{aligned} \tag{2.21}$$

$$\begin{aligned}\left\langle (y(t)-y_0)^2 \right\rangle =& v^2 \int_0^t \mathrm{d}t_1 \int_0^t \mathrm{d}t_2 \left\langle \sin\theta\left(t_1\right)\sin\theta\left(t_2\right)\right\rangle \\ &+ \frac{2v}{\gamma}\int_0^t \mathrm{d}t_1 \int_0^t \mathrm{d}t_2 \left\langle \sin\theta\left(t_1\right)\xi_y\left(t_2\right)\right\rangle + \frac{1}{\gamma^2}\int_0^t \mathrm{d}t_1 \int_0^t \mathrm{d}t_2 \left\langle \xi_y\left(t_1\right)\xi_y(t_2)\right\rangle.\end{aligned} \tag{2.22}$$

The second and third terms were already solved for the passive particles and the results are zero and $2D_T t$, respectively. To calculate the first integral in 2.21, we notice that:

$$\langle \cos\theta_1 \cos\theta_2\rangle = \langle \cos\theta_1 \cos\theta_2\rangle_{t_1>t_2} + \langle \cos\theta_1 \cos\theta_2\rangle_{t_2>t_1}\,, \tag{2.23}$$

and that

$$\langle \cos\theta_1 \cos\theta_2\rangle_{t_1>t_2} = \int d\theta_1 \int d\theta_2 \cos\theta_1 \cos\theta_2 e^{\frac{-(\theta_1-\theta_2)^2}{4D_R(t_1-t_2)}} e^{\frac{-(\theta_2-\theta_0)^2}{4D_R t_2}}. \tag{2.24}$$

Assuming $\theta_0 = 0$, and integrating over $d\theta_1$, by using the result in the Appendix with $\phi_0 = \theta_2$, $\alpha = 1$ and $\sigma^2 = 2D_R(t1 - t2)$, we obtain:

$$\begin{aligned}& e^{-D_R(t1-t2)}\int_{-\infty}^{+\infty} d\theta_2 \cos^2\theta_2 \frac{1}{\sqrt{4\pi D_R t_2}} e^{\frac{-\theta_2^2}{4D_R t_2}} = \\ &= e^{-D_R(t1-t2)}\int_{-\infty}^{+\infty} d\theta_2 \frac{1}{2}(1+\cos(2\theta_2))\frac{1}{\sqrt{4\pi D_R t_2}} e^{\frac{-\theta_2^2}{4D_R t_2}} = \\ &= e^{-D_R(t1-t2)}\frac{1}{2}\Big[\int_{-\infty}^{+\infty} d\theta_2 \frac{1}{\sqrt{4\pi D_R t_2}} e^{\frac{-\theta_2^2}{4D_R t_2}} + \int_{-\infty}^{+\infty} d\theta_2 \frac{1}{\sqrt{4\pi D_R t_2}} e^{\frac{-\theta^2}{4D_R t_2}}\cos(2\theta_2)\Big] = \\ &= e^{-D_R(t1-t2)}\frac{1}{2}\Big[1 + \int_{-\infty}^{+\infty} d\theta_2 \frac{1}{\sqrt{4\pi D_R t_2}} e^{\frac{-\theta_2^2}{4D_R t_2}}\cos(2\theta_2)\Big].\end{aligned} \tag{2.25}$$

This last integral can again be solved using the result in the appendix with $\alpha = 2$, $\phi_0 = 0$ and $\sigma^2 = 2D_R t_2$. Accordingly, we get:

$$\langle \cos\theta_1 \cos\theta_2\rangle_{t_1>t_2} = \frac{1}{2} e^{-D_{\mathrm{R}}(t_1-t_2)}\left[1 + e^{-4D_{\mathrm{R}}t_2}\right]. \tag{2.26}$$

Proceeding in the same way for $\langle \cos\theta_1 \cos\theta_2\rangle_{t_2>t_1}$ we get the same expression with t_1 and t_2 switched.

The first integral in 2.21 can then be rewritten as

$$v^2 \int_0^t dt_1 \int_0^{t1} dt_2 \frac{1}{2} e^{-D_R(t_1-t_2)} \left[1 + e^{-4D_R t_2}\right] + v^2 \int_0^t dt_2 \int_0^{t2} dt_1 \frac{1}{2} e^{-D_R(t_2-t_1)} \left[1 + e^{-4D_R t_1}\right]. \tag{2.27}$$

Performing the integration we obtain

$$\left\langle (x(t))^2 \right\rangle = 2D_T t + \frac{v^2}{D_R^2} \left[e^{-D_R t} + D_{\mathrm{R}} t - 1 + \frac{1}{12} \left(e^{-4D_{\mathrm{R}} t} - 4e^{-D_{\mathrm{R}} t} + 3 \right) \right]. \tag{2.28}$$

Following the same procedure for the y component we obtain

$$\left\langle (y(t))^2 \right\rangle = 2D_T t + \frac{v^2}{D_R^2} \left[e^{-D_R t} + D_{\mathrm{R}} t - 1 - \frac{1}{12} \left(e^{-4D_R t} - 4e^{-D_R t} + 3 \right) \right]. \tag{2.29}$$

Thus, the mean square displacement is

$$\mathrm{MSD}(t) = \left[4D_{\mathrm{T}} + 2v^2 t_{\mathrm{R}}\right] t + 2v^2 t_{\mathrm{R}}^2 \left[e^{-t/t_{\mathrm{R}}} - 1 \right]. \tag{2.30}$$

Comparing the expression for the mean squared displacement of an active Brownian particle in an overdamped regime [Eq. (2.30)] with the one deduced for a passive one [Eq. (2.10)], we see that both are characterized by a ballistic behavior at short times and diffusive one for long times, however, the effective diffusion coefficients are different. While for the passive particles this is set by the ratio between the thermal energy of the fluid $k_B T$ and the Stokes coefficient γ, in the case of an active agent, this coefficient is set by the sum of the passive one and an additional term that results from the activity. The time scale for the two different regimes is also different. In fact, if we consider the overdamped regime for both cases $\frac{m}{\gamma} \to 0$, looking at time scales much larger than this "passive typical time", we see that the active agents still show ballistic behavior for $t \approx \tau_R$. This can be seen by performing a polynomial expansion of the Eq. (2.30) near the point $t = 0$:

$$\mathrm{MSD}(t) = (4D_{\mathrm{T}} + 2v^2\tau_R)t + 2v^2(1 - t\tau_R + \frac{t^2\tau_R^2}{2} + O(t^3) - 1) \approx 4D_T t + v^2 t^2. \tag{2.31}$$

For times $t >> \tau_R$ the exponential term goes to zero and the active particles behave in a diffusive manner,

$$\mathrm{MSD}(t) = \left[4D_{\mathrm{T}} + 2v^2\tau_{\mathrm{R}}\right] t = 4D_{\mathrm{eff}} t, \tag{2.32}$$

where we can assume an effective enhanced diffusion $D_{\mathrm{eff}} = D_T + \frac{1}{2}v^2\tau_R$. This means that, while for a passive particle with radius $R = 1$ μm in water the diffusive behavior is observed for times much larger than 10^{-3} s, for an active particle in the same conditions, this kind of motion will only be observed for times much larger than $\tau_R \approx 6$ s [1]. In spite of the apparent similarities that may suggest that active systems can be regarded, asymptotically, as equilibrium systems at a higher effective temperature (that leads to a higher a diffusion coefficient), if interactions between particles start to be non-negligible or if the environment is heterogeneous, typical behaviors found at equilibrium are not recovered. It has been observed for example, experimentally and numerically, a non-uniform spatial distribution of particles in

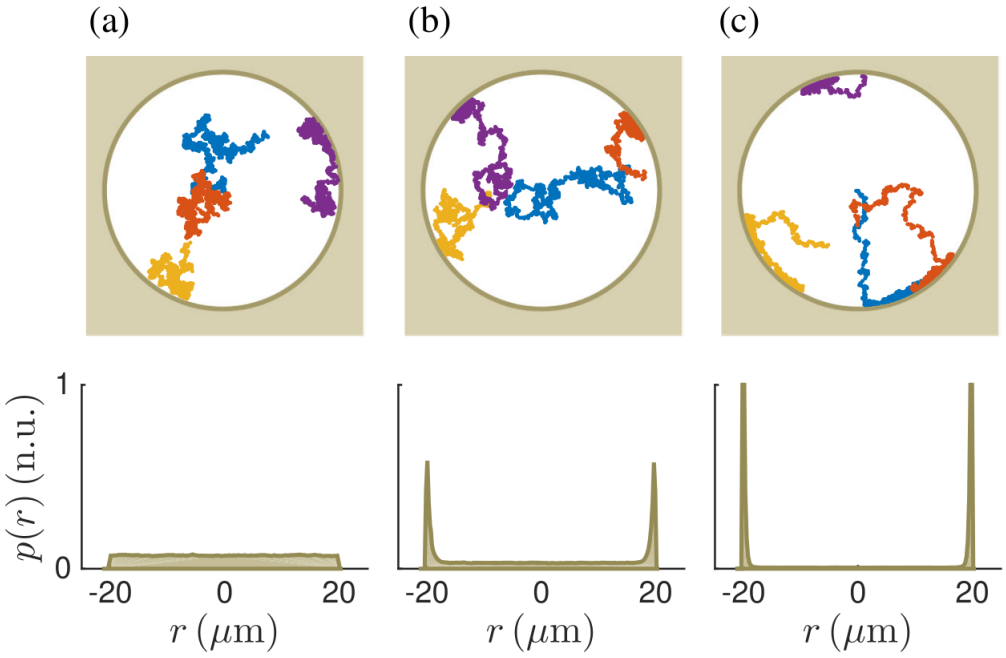

Figure 2.1: Position distributions for active particles in a pore. (a) - (c) Simulated trajectories (solid lines) of active Brownian particles circular pore with reflective boundaries at velocity (a) passive Brownian motion, (b) active Brownian particle, (c) same as (b) but particles have higher velocity. The bottom show the probability distribution along a diameter of the circular pore: uniform across the whole pore in the case of passive Brownian particles, the probability increases toward the walls in the case of active Brownian particles together with the particle velocity. Figure and caption adapted from [1].

confined geometries such as a circular pore (Fig.2.1), since an asymmetry between the mechanism that takes them toward and away from the the walls i.e, directed motion (governed by the linear velocity of the active particle, v) and diffusion (governed by D_R and D_T) will cause the tendency for particles to accumulate at the boundaries. One other important phenomenon observed in systems whose agents are active and not observed for a dilute solution of passive Brownian particles is the spontaneous formation of clusters without the need for attractive interactions, a phenomenon known as motility induced phase separation (MIPS) [1].

Chapter 3

Chiral active motion

Up to now, we considered only the ideal case of non-chiral active Brownian motion. However, if by some reason it happens to exist an asymmetry on the particle's shape or propulsion mechanism the particle will have a tendency to shift its preferential direction towards one of the sides. This will lead to circular trajectories in two dimensions and helical ones in three. This kind of movement is characteristic of many flagellated bacteria when moving close to a surface, such as the *E.coli* [22] [9] , *V. alginolyticus* [19], and *C. crescentus* [24], Fig. 3.1.

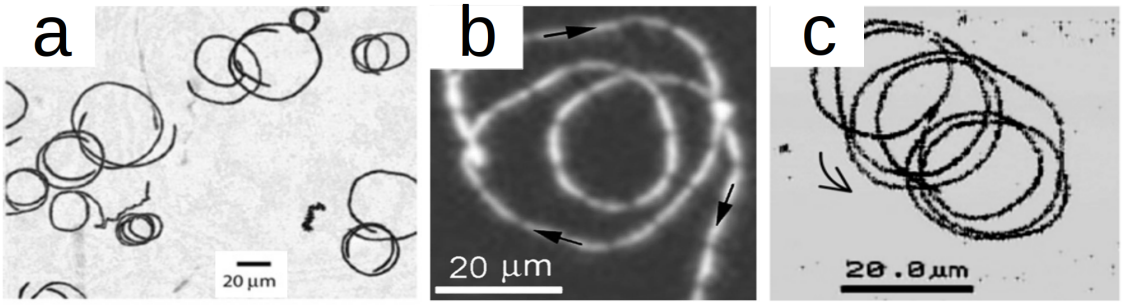

Figure 3.1: Examples of chiral motion for flagellated bacteria moving near to surfaces. (a) *E.coli* (taken from [22]. (b) *C. crescentus* (taken from [24]). (c) *V. alginolyticus* (taken from [19]).

The change of behavior when moving close to a surface alters the proliferation of these organisms and affects not only the motility but also the adhesion to surfaces since a circular swimmer will tend to spend more times in a surface than a "straight" swimmer [3].

Chiral motion has not only been observed in flagellated bacteria but also in spermatozoa cells swimming near a substrate [41], for magnetotactic bacteria that orient themselves along the lines of Earth's magnetic field [7] and also for artificial swimmers [20].

In the following section, we describe a recent experiment performed by Stanislaw Makarchuk, Lena Ciric and Giorgio Volpe at the University College of London. The purpose was to study the influence of the micro-environment in the motion of individual chiral swimmers. They show that micro-obstacles influence the propagation of peritrichously flagellated bacteria on a flat surface in a non-monotonic way. Instead of hindering it as shown for non-chiral active bacteria in Ref.[25], there is an optimal density for which cells' propagation is significantly enhanced.

In their experiments they used as model organism the *Escherichia coli*, a flagellated bacteria which is able to self-propel. These bacteria are considered to be among the most studied organisms in the world

for several reasons. They grow very quickly, in chemically defined environments, and are relatively cheap. This organism is also able to reproduce fast and there is an extensive knowledge accumulated over the years about many of their properties, such as genetic characteristics and mechanical properties like the mechanism used for self propulsion [2].

The self-propulsion of these organisms happens due to the many flagella on the bacteria body that arrange in a cork like manner and that by rotating, in a non-reciprocal way, allow the bacteria to move in viscous fluids [2]. The hydrodynamic interactions with the substrate that lead to chiral motion, arise because when the bacteria is near a substrate there is a difference between the viscous forces felt in the side turned to the surface and the other one. Since the flagellum rotates in a direction opposite to the rotation of the body, each will feel a force to opposite sides, and thus, the bacteria will feel a net torque. This torque will cause the cell to swim clockwise if it is near a bottom surface and anti-clockwise if it is near a top surface, when viewed from above [22] [21].

3.1 Experiments

Experimental setup

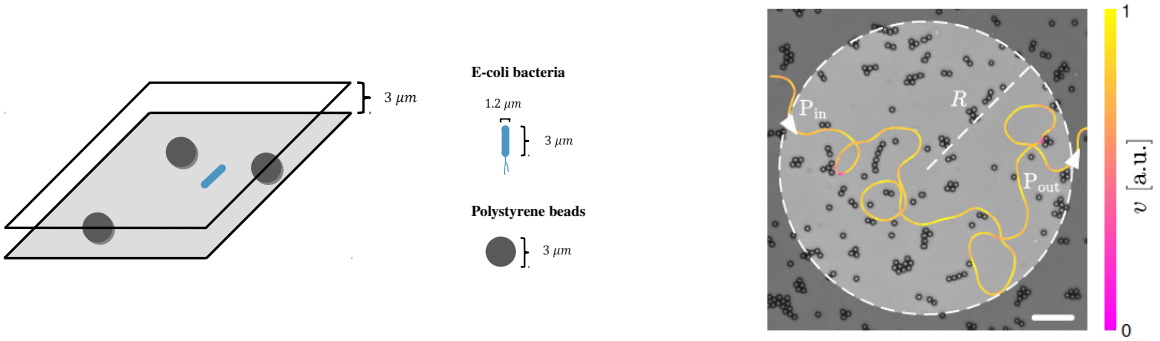

Figure 3.2: Left :scheme of the experimental setup. Right: Example of an *E. coli* cell's trajectory near a surface with fixed obstacles. The colour code represents the instantaneous velocity v of the trajectory normalized to its maximum value. The white dashed line delimits a circular area of radius R in the total field of view and intersects the trajectory at points P_{in} and P_{out} , which respectively represent the points of entrance and exit of the cell in the circular area. This geometrical configuration is used for the calculation of the average effective propagation distance L_{eff} in Fig. 3.3.

To investigate the effect of the micro-environment in the dynamics of micro-swimmers the group led by Dr. Giorgio Volpe placed *E.coli* enclosed by chambers made of two microscopy cover-slips separated by polystyrene beads (diameter $d \approx 2.99\mu$m) as spacers, thus effectively confining them to a quasi-2D geometry. By controlling the initial concentration of the colloidal dispersion used to prepare the chamber, it was then possible to produce quasi-2D random micro-environments with different densities ρ of fixed obstacles in the range from $\rho = 0\%$ to $\rho = 12\%$.

The average translational and angular velocities of the motile bacteria during a run event (motion along a straight line) were estimated to be $\Omega_0 = 0.8$ rad s^{-1} and $< v >= 10.95$ μm s^{-1} .

They analyzed the trajectories of the particles in a circular region with varying obstacle density. In the analysis, all the trajectories that did not exit the circle after entering it were excluded as well as

trajectories with penetration depth lower than 10% of the the circle diameter without interacting with the obstacles.

Experimental results

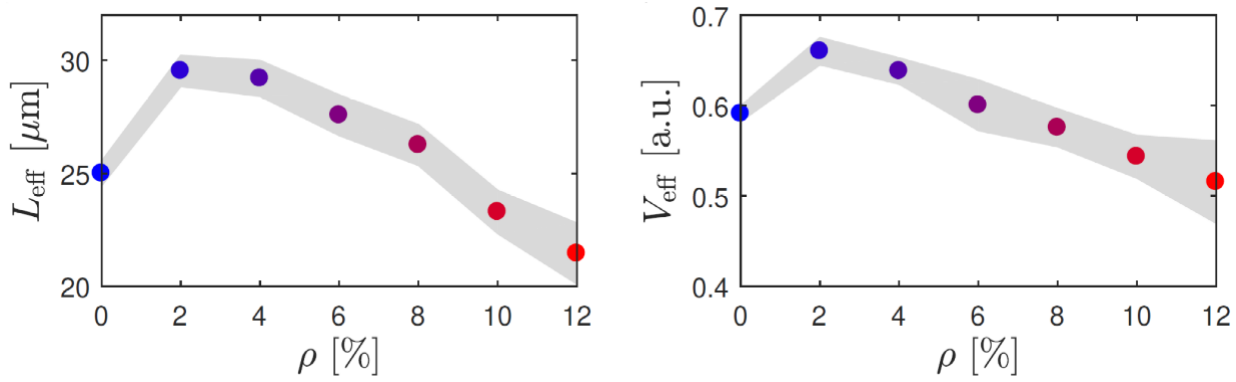

Figure 3.3: Average effective propagation distance L_{eff} and speed V_{eff} as a function of the obstacle density ρ for a circular area of radius $R = 25$ μm. Each value is obtained from averaging at least 1000 different trajectories. The shaded area around the average values are delimited by one standard deviation.

For each bacterium that effectively propagates through these areas was defined an effective propagation distance $\ell_{\text{eff}} = |\vec{P}_{out} - \vec{P}_{in}|$. Where $\vec{P}_{in}$ and $\vec{P}_{out}$ correspond respectively to the entrance and exit point of the circular region (Fig. 3.2, left). This measurement can take any value between 0 (the bacterium exits from where it entered) and $2R$ (the bacterium crosses the whole circle exiting at the diametrically opposite point from where it entered). Averaging this value over all bacteria that propagate through any area of given density ρ, it's possible to calculate an average effective propagation distance $L_{\text{eff}} = \langle l_{\text{eff}} \rangle$ as a function of obstacle density as plotted in Fig. 3.3.

In the absence of obstacles, they found $L_{\text{eff}} \approx R = 25$ μm, meaning that the bacteria, consistently with their chirality, do not propagate beyond half circle on average.

An interesting behavior is observed when obstacles are introduced. It would be expected that as the obstacle density increases, the average effective spreading of the bacteria would decrease due to the augment in the number of collisions, however, it is observed that for values of ρ between $\rho = 2\%$ and $\rho = 8\%$ there is in fact an increase in the value of L_{eff} indicating that on average the particles are able to cover larger distances. The expected behavior (a decrease of L_{eff} with an increase in ρ over the case $\rho = 0\%$) is only recovered for high obstacle densities ($\rho > 8\%$). Interestingly, for the optimal value ($\rho = 2\%$), L_{eff} is 20% higher than the value for $\rho = 0\%$.

These results suggest that, the chiral motion of the bacteria is rectified, increasing their motility.

Since the presence of obstacles should also affect the time spent inside the circle, the group also measured the normalized average effective velocity. The effective velocity of a single cell is taken to be the effective distance l_{eff} of a sub-trajectory divided by the duration. The average effective velocity is then $V_{\text{eff}} = \langle \frac{v_i}{Tv} \rangle$ with v_i and T respectively being the average velocity and duration of the sub-trajectory within the circle.

The same non-monotonic behavior can be observed for the mean normalized effective velocity of the bacteria V_{eff} (Fig. 3.3). This tendency shows that not only the bacteria are able to travel larger distances but also that they are able to do it effectively faster. However, it is noted that for $\rho > 4\%$ the value of V_{eff} is lower than in the case where we have no obstacles (whereas for L_{eff} this is only observed for $\rho > 8\%$).

This indicates that for this obstacle concentration although they travel longer distances, the particles take longer to leave the circular region of analysis.

To try to explain this counter-intuitive behavior, it was also calculated the probability distribution of the overall change in directionality $\Delta\theta = |\theta_{out} - \theta_{in}|$, for different values of ρ (3.4), where $\Delta\theta$ is the angle between the tangents to a cell's trajectory when exiting and entering a circular area, respectively.

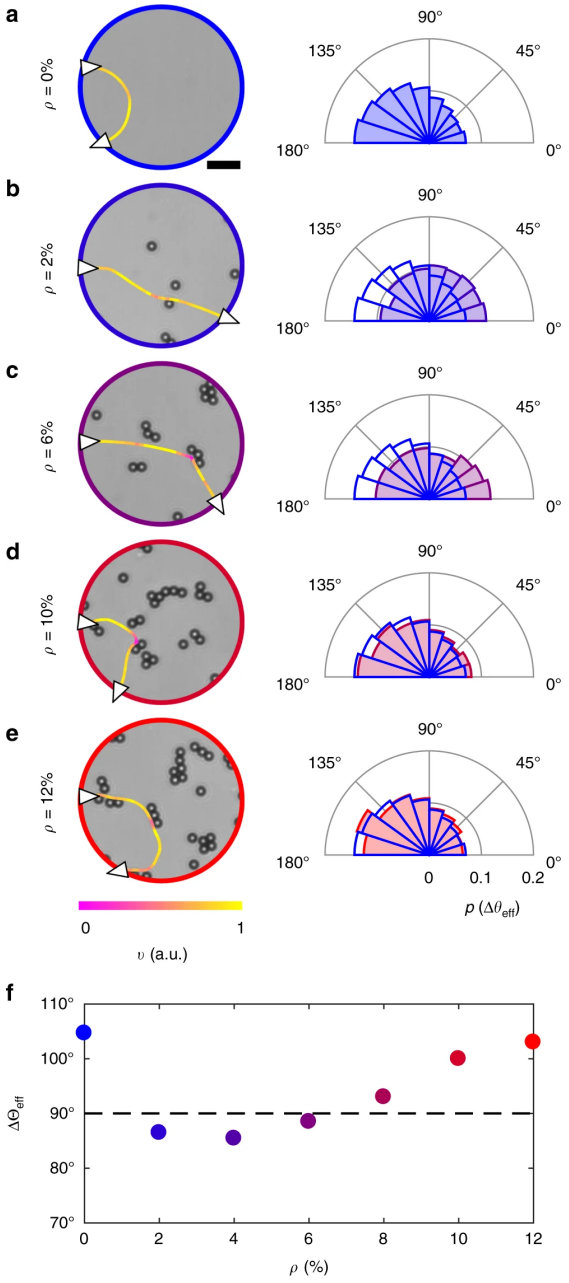

Figure 3.4: Change in effective propagation direction for *E. coli* cells near a surface with obstacles. (a-e) Exemplary trajectories and probability distributions of the change in effective propagation direction Θ_{eff} for *E. coli* cells swimming through a circular area of $R = 25$ μm for different obstacle densities ρ. In the distributions, $\Theta_{\text{eff}} = 90^\circ$ separates between forward ($\Theta_{\text{eff}} < 90^\circ$) and backward ($\Theta_{\text{eff}} > 90^\circ$) propagation respectively. For reference, the distribution in (a) is also shown in (b-e) as a solid line. (f) Average change in effective propagation direction Θ_{eff} as a function of ρ calculated from the previous probability distributions. The dashed line represents the separation between forward and backward propagation at 90°.

Here, $\Delta\theta = 0^\circ$ represents the tendency of bacteria to move perfectly forward (i.e. bacteria keep their directionality from entrance to exit point), while $\Delta\theta = 180^\circ$ represents the tendency of bacteria to move perfectly backward (i.e. bacteria turn back on themselves from entrance to exit point), with $\Delta\theta = 90^\circ$ as

the separation point between the two cases. From this is possible to gain a better qualitative understanding of the behavior of each particle. In the case where the environment is free of obstacles, the trajectories return predominantly backwards due to the chiral character of the movement of the particles and so they observed a high value for the average change in propagation distance, $\Theta_{\text{eff}} =< \Delta\theta >\approx 100°$, Fig. 3.4f. By slightly increasing the number of obstacles, we see a decrease in the value of Θ_{eff} indicating that on average trajectories are more like straight lines due to a decrease of the typical radius of curvature of the trajectories. This behavior is illustrated by Fig. 3.4(a-c). If the density of obstacles is further increased, naturally, the bacteria will be blocked more often and need to return back on its trajectory most of the times, as illustrated in Fig. 3.4(d-e).

The group also performed an analysis of the effect of the radius of the region of measurement to see how the mentioned behavior scales when changing the size of the area of interest, as shown in Fig. 3.5. A quick analysis of the figure allows us to check that V_{eff} is optimal in the absence of obstacles for very small areas ($R = 5$ μm, i.e. $2R \leq r_C$). On the other hand, it is also clear the lowering of the absolute value of V_{eff} for increasing R. This behavior is due to a decreasing of L_{eff} and an increase of the time spent within the area due to its larger size. In spite of this, is interesting to notice that the behavior is preserved over long distances, even at $R = 50$ μm, bacteria still propagate better in the presence of a few obstacles.

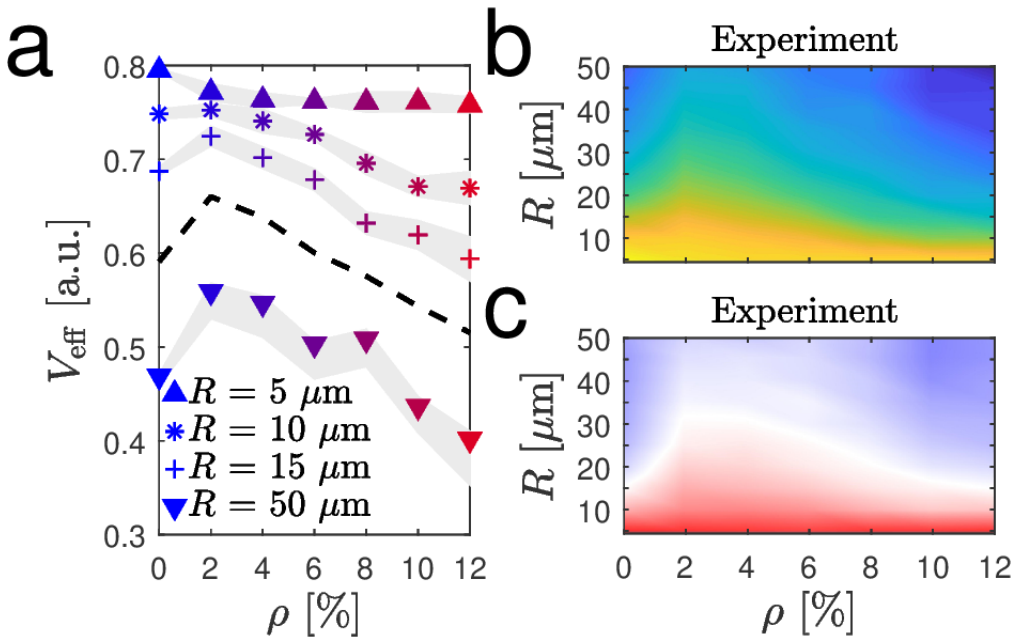

Figure 3.5: (a) Average effective propagation speed V_{eff} as a function of obstacle density for $R = 5, 10, 15, 50$ μm. (b) Colormap of average effective speed as a function of obstacle density inside the circle and its radius. (c) Colormap of average angle change after passing the circle as function of obstacle density and circle radius.

All of this experimental results seem to show that there is, for a certain amount of time, a reduction of the angular velocity of the bacteria when they interact with an obstacle. This interpretation is also corroborated by the observation of a change of the bacteria distance to the closest surface when interacting with an obstacle, Fig. 3.6(a,b). In Fig. 3.6(a) we see also, that when the bacteria is swimming on the right side, meaning that is near the top surface, and approaches an obstacle from the right, its chirality changes as it would be expected if the bacteria is (after this scattering interaction) approaching the bottom surface. The last observation seem also to suggest that the interaction with the obstacle is similar to the ones with the surface since the bacteria tends to the bottom surface when the obstacle it is

interacting with is on its right (with respect to the direction of motion) and only going up again when an obstacle is to its left.

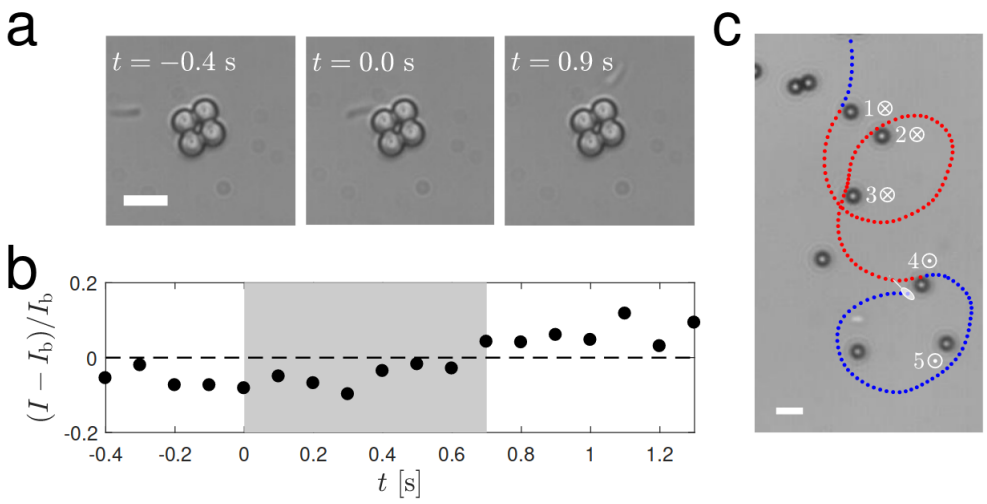

Figure 3.6: Change of *E. coli* cells' distance from the surface after forward scattering. (a) Time lapse sequence of an *E. coli* cell swimming near an obstacle on the sample chamber's bottom surface during a forward-scattering event. These sequence was acquired using a 40x microscope objective (NA = 0.75, Leica HCX PL Fluotar). The cell-obstacle interaction starts at t = 0 s. The white scale bar corresponds to 5 μm. (b) Relative change in the average gray-scale intensity I of the cell image with respect to the background value I b (dashed horizontal line). As soon as the cell has crossed the obstacle, its distance from the surface changes as qualitatively highlighted by the fact that I goes from being darker than the background to being brighter. The gray shaded area highlights the duration of the cell-obstacle interaction. (c) Exemplary trajectory showing 5 forward-scattering events, where the stylized cell represents the trajectory's final position and direction of motion: initially, the cell is near the sample chamber's top surface as shown by the fact that it appears to swim clockwise (blue) in our setup; the cell's distance from the surface changes every time it passes an obstacle from its side where the consequent hydrodynamic torque points the cell towards the opposite surface, i.e upwards when near the bottom surface (4) and downwards when near the top surface (1); the cell's distance from the closer surface does not change otherwise (2,3,5). When the swimming cell changes surface of the sample chamber, the sign of the trajectory's chirality switches from clockwise (blue) to counterclockwise (red), and vice versa. The white scale bar corresponds to 5 μm.

The mentioned behaviors suggest that, besides the natural repulsive interactions with the obstacles, the bacteria are subjected to an extra one that tends to rectify the trajectories by locally reducing the angular velocity. This non-monotonic behavior might then be explained as an interplay between collisions and forward scattering events. Following this interpretation, for a low number of obstacles the swimmers experience few collisions but a sufficiently high number of forward scatterings as to increase their mobility. On the other hand, for a high number of obstacles the forward scatterings no longer compensate the number of collisions, and the trajectories get more localized.

3.2 Model

3.2.1 Langevin equation for chiral active particles

Inspired by these experiments we came up with a simple numeric model for active chiral particles in an environment filled with obstacles. We tried to keep the model as simple as possible while keeping the minimum ingredients necessary to reproduce the experimental observations presented. In particular we aimed at understanding the non monotonic behavior in effective distance L_{eff} and effective distance V_{eff}. Generally, the *E.coli* motion is modeled numerically using a Run-And-Tumble model [1]. This model has similar results to the active Brownian particles we referred earlier and recovers the same kind of MSD deduced. Since we want to show that the non-monotonic behavior is not a particular feature of this system but a more general result for systems of chiral swimmers where, besides collisions with the obstacles, there is a forward-scattering kind of interaction with micro-obstacles that fill the environment, we will use the framework of active Brownian particles by solving the corresponding Langevin equation.

The chiral nature of an active particle can be introduced in the Langevin equation by considering an extra angular velocity term Ω_0 to the equation of motion for the angle θ.

We neglect the fact that the actual cells have a cylinder like shape (sphero-cylinder in 3-D) and take the bacteria to be two dimensional disks. We consider that the bacteria moves in circular like trajectories with angular velocity Ω_0 in the absence of obstacles, and neglect the effect of the thermal fluctuations in the translational degrees of freedom keeping only the term for the random torques that influence the bacteria's preferential direction.

In the absence of obstacles the trajectory of each bacterium is obtained integrating the Langevin equations, in the overdamped regime,

$$\frac{dx(t)}{dt} = v\cos\theta(t), \tag{3.1}$$

$$\frac{y(t)}{dt} = v\sin\theta(t), \tag{3.2}$$

$$\frac{d\theta(t)}{dt} = \xi_\theta + \Omega_0. \tag{3.3}$$

Using the same methods as before and assuming ($x(t=0)=0$, $y(t=0)=0$) we can now find the first moments of $x(t)$, $y(t)$ and $\theta(t)$:

$$\langle\theta(t)\rangle = \theta_0 + \Omega_0 t \tag{3.4}$$

$$\begin{aligned}\langle x(t)-x_0\rangle =& \frac{v}{\left(D_{\text{R}}^2+\Omega_0^2\right)}\left[D_{\text{R}}\cos\left(\theta_0\right)-\Omega_0\sin\left(\theta_0\right)\right.\\ &\left.+\,e^{-D_{\text{R}}t}\{\Omega_0\sin\left(\theta_0+\Omega_0 t\right)-D_{\text{R}}\cos\left(\theta_0+\Omega_0 t\right)\}\right]\end{aligned} \tag{3.5}$$

$$\begin{aligned}\langle y(t)-y_0\rangle =& \frac{v}{\left(D_{\text{R}}^2+\Omega_0^2\right)}\left[D_{\text{R}}\sin\left(\theta_0\right)+\Omega_0\cos\left(\theta_0\right)\right.\\ &\left.-\,e^{D_{\text{R}}t}\{D_{\text{R}}\sin\left(\theta_0+\Omega_0 t\right)+\Omega_0\cos\left(\theta_0+\Omega_0 t\right)\}\right].\end{aligned} \tag{3.6}$$

These trajectories correspond to a logarithmic spiral [35] and can be observed in Fig. 3.9. As for the mean square displacement we have to calculate $\langle\cos(t1)\cos(t2)\rangle$ and $\langle\sin(t1)\sin(t2)\rangle$. We notice that now,

$$P(\theta_1|\theta_2) = \frac{1}{\sqrt{4\pi D_{\mathrm{R}}\left(t_1 - t_2\right)}} \exp\left(-\frac{\left[\theta_1 - \theta_2 - \Omega_0\left(t_1 - t_2\right)\right]^2}{4D_{\mathrm{R}}\left(t_1 - t_2\right)}\right), \tag{3.7}$$

and so

$$\langle \cos\theta_1 \cos\theta_2 \rangle_{t_1 > t_2} = \frac{1}{2} e^{-D_{\mathrm{R}}(t_1 - t_2)} \left[\cos\{\Omega_0\left(t_1 - t_2\right)\} + \cos\{2\theta_0 + \Omega_0\left(t_1 + t_2\right)\} e^{-4D_{\mathrm{R}} t_2}\right], \tag{3.8}$$

$$\langle \sin\theta_1 \sin\theta_2 \rangle_{t_1 > t_2} = \frac{1}{2} e^{-D_{\mathrm{R}}(t_1 - t_2)} \left[\cos\{(\Omega_0\left(t_1 - t_2\right)\} - \cos\{(2\theta_0 + \Omega_0\left(t_1 + t_2\right)\} e^{-4D_{\mathrm{R}} t_2}\right]. \tag{3.9}$$

Since the last two terms of both expressions have opposite signs, they will cancel and we only need to consider the first term in the integral. Thus, we have

$$\mathrm{MSD}(t) = 2v^2 \int_0^t dt_1 \int_0^{t_1} dt_2 e^{-D_R(t_1 - t_2)} \cos[\Omega_0(t_1 - t_2)]. \tag{3.10}$$

Finally, performing the integration we obtain

$$\mathrm{MSD}(t) = \frac{2v^2}{(D_R^2 + \Omega_0^2)^2} \Big[(\Omega_0^2 - D_R^2 + D_R\left(D_R^2 + \Omega_0^2\right) t) + e^{-D_R t}\{(D_R^2 - \Omega_0^2)\cos(\Omega_0 t) - 2D_R\Omega_0 \sin(\Omega_0 t)\}\Big]. \tag{3.11}$$

Once again, we notice that near the point t=0,

$$\mathrm{MSD}(t = 0) \approx v^2 t^2 + O(3). \tag{3.12}$$

and in the asymptotic limit we have a purely diffusive behavior:

$$\mathrm{MSD}(t \to \infty) \approx \frac{2v^2\Big[\Omega_0^2 - D_R^2 + D_R(D_R^2 + \Omega_0^2)t\Big]}{(D_R^2 + \Omega_0^2)^2}. \tag{3.13}$$

To try to reproduce the experimental results, we improved this model by adding the interactions of the bacteria with the obstacles. For simplicity we assume that the bacteria interacts only with closest obstacle and describe the cell-obstacle interaction as a superposition of three contributions: a repulsive interaction $\vec{F}_i$, forward-scattering $\Omega_i(r)$ and random reorientation upon tumble-collision. We modeled the first by introducing a repulsive force in the equation of motion. This force depends on the particle's distance r_i from the nearest obstacle as

$$\vec{F}_i\left(r_i\right) = \frac{e^{-r_i}}{|r_i - d|}\hat{\mathbf{r}}_i. \tag{3.14}$$

This function was chosen to reproduce a strong (local) repulsive interaction between particle and obstacle, i.e. to mimic a hardcore potential. The exponential term ensures that the force does not increase too abruptly when approaching the obstacle, which is convenient to avoid numerical instabilities.

To model the forward-scattering (the second contribution), we introduced a position dependent angular speed. Since the proximity to the substrate causes a bias in the movement of the particles which causes the chiral motion, expressed by the term $\Omega_i(r)$, and considering as our hypothesis that the active particles move away from the substrate by interacting locally with an obstacle, the loss of chirality (i.e,

angular velocity) is modeled considering an extra interaction with the closest obstacle given by:

$$\Omega_i\left(r_i\right) = \Omega_0\left(1 - e^{-\frac{r_i - d}{r_1}}\right). \tag{3.15}$$

Ω_0 corresponds to the value of the deterministic angular velocity when the particles are far from obstacles, $r_i = |\vec{r}_i - \vec{r}_o|$ is the distance between particle and obstacle, r_1 is a constant that sets a length scale for the interaction and d corresponds to the particle's and obstacle's diameters. Note that in the absence of obstacles the angular velocity will be Ω_0 and when the bacteria touches the obstacle (at $r = 2r_0$) the angular velocity is zero and the bacteria swims in straight lines.

Finally, any time the particle's speed drops below $v_i/100$ a uniformly generated random angle in the interval $[\pi/2, 3\pi/2]$ is added to θ to better reproduce the experimental case of tumble-collisions (the third contribution).

Having all of this into account, the trajectory of each particle is obtained by integrating the overdamped Langevin equation

$$\frac{d\vec{r}_i}{dt} = \frac{\vec{F}_i(r)}{\gamma} + v\vec{u}, \tag{3.16}$$

where, $\vec{r}_i$ is the position of particle i, F_i is the force acting on the particle i due to its closest obstacle, γ_i is the Stokes coefficient, v is the speed of the active particle $\vec{u}$ is the unitary vector $(\cos(\theta_i), \sin(\theta_i))$ where θ_i is the solution of the stochastic equation:

$$\frac{d\vec{\theta_i}}{dt} = \sqrt{2D_R}\xi_\theta + \Omega_i(r), \tag{3.17}$$

where $D_R = \frac{k_B T}{8\pi\eta R^3}$ corresponds to the particle's rotational diffusion constant and $\Omega_i(r)$ the extra term that relates to an additional deterministic angular velocity that expresses the chirality of the particles.

3.2.2 Numeric simulations

Equations (3.16) and (3.17) are integrated using a second-order stochastic Runge-Kutta numerical scheme. The discrete form of the equations is

$$\begin{aligned} \vec{r}_i'(t) &= \vec{r}_i(t) + \vec{F}_i\left(\vec{r}_i(t)\right)\frac{\Delta t}{\gamma} + v\vec{u'}\Delta t \\ \vec{r}_i(t+\Delta t) &= \vec{r}_i(t) + \left[\vec{F}_i\left(\vec{r}_i(t)\right) + \vec{F}_i\left(\vec{r}_i'(t)\right)\right]\frac{\Delta t}{2\gamma} + v\vec{u}\Delta t \end{aligned}, \tag{3.18}$$

$$\begin{aligned} \theta_i'(t) &= \theta_i(t) + \Omega_i\left(\vec{r}_i(t)\right)\frac{\Delta t}{\gamma} + \xi_{\theta_i} \\ \theta_i(t+\Delta t) &= \theta_i(t) + \left[\Omega_i\left(\vec{r}_i(t)\right) + \Omega_i\left(\vec{r}_i'(t)\right)\right]\frac{\Delta t}{2} + \xi_{\theta i} \end{aligned}. \tag{3.19}$$

The time step is chosen to be $\Delta t = 10^{-4}$ s. All parameters were chosen to closely follow the experimental parameters, the radii of both obstacles and bacteria is $r_0 = 1.5$ μm, the typical length of interaction $l = 10.7$ μm. The linear and angular velocities of the swimmers were chosen as the average of the all ensemble , $\Omega_0 = 0.8$ rad/s and $v = 10.95$ m/s. The value for the rotational diffusion constant was chosen to better reproduce quantitatively the experimental results $D_R = 0.225$ rad^2/s. The box size is $L = 59$ μm, periodic boundary conditions were used.

Since the fluid is considered to be in thermodynamic equilibrium at a thermostat temperature T and hydrodynamic effects are neglected, the time series of the stochastic force is drawn from a Gaussian distribution with zero mean value and uncorrelated second moment in time and space, given by

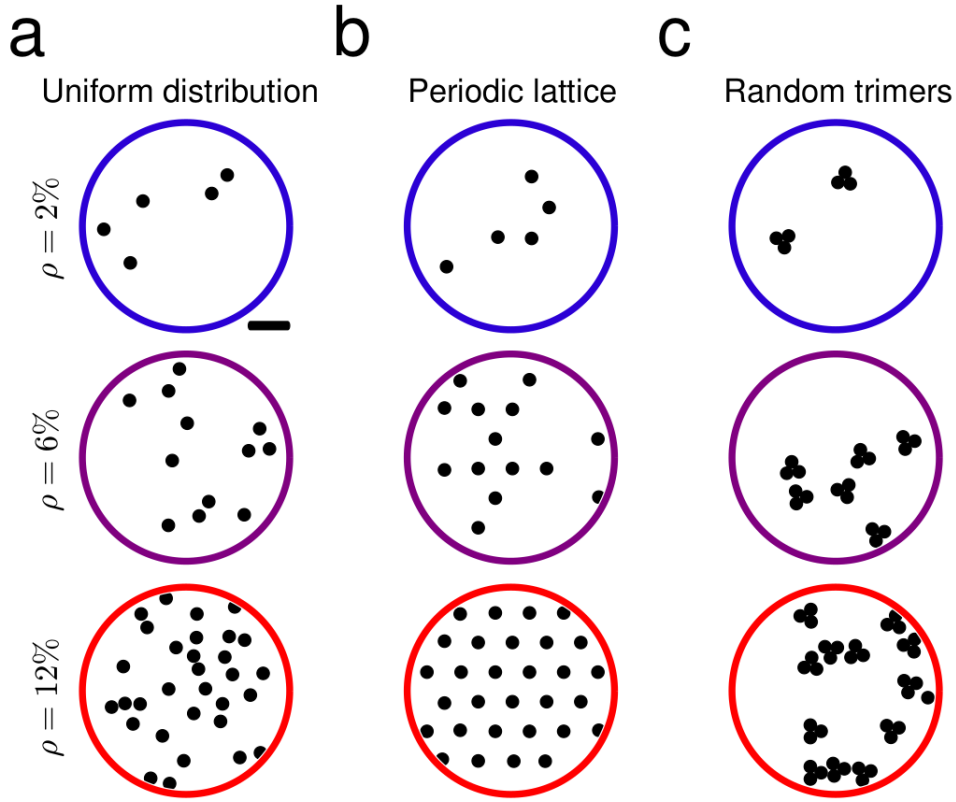

Figure 3.7: Simulated distributions of obstacles. (a-c) Examples of different simulated obstacle distributions in a circular area of radius$R = 25$ μm for increasing obstacle densities ρ. Individual obstacles are deposited (a) sequentially at random without overlap, (b) according to a periodic lattice and (c) sequentially as non-overlapping trimers (i.e.triangular clusters of obstacles) with a random orientation. In b, $\rho = 12\%$ corresponds to a complete lattice and lower obstacle densities are obtained by removing particles at random. The black scale bar corresponds to 10 μm.

$\left\langle \xi_\theta^k(t)\xi_\theta^l(t')\right\rangle = \delta_{kl}\delta(t-t')$.

We varied the density of obstacles ρ and measured the effective velocity. To test the robustness of our results, different obstacle configurations were considered. We place circular obstacles with variable densities ρ deposited sequentially at random without overlap (Fig. 3.7a), according to a periodic triangular lattice (lattice constant equal to 2.75d) where $\rho = 12\%$ corresponds to a complete lattice and lower obstacle densities are obtained by removing particles uniformly at random (Fig. 3.7b), or sequentially as non-overlapping trimers (i.e. triangular clusters of obstacles) with a random orientation (Fig. 3.7c).

3.2.3 Code Validation

In Fig. 3.8 we show the trajectories obtained for 100 particles, that start at the same point $(x = 0, y = 0)$ with the same initial orientation $(\theta = 0)$ for 4 different instant of times $(t = 1, 2, 5, 10$ s). In the first snapshot ($t = 1$ s) we see that even tough the swimmers start with the same initial orientation, after some time this preferential direction gets randomized and the particles depart from the initial point in different directions. In the last snapshot we see that the particle's directions has already diffused considerably and they all spread around the same point (different from the initial one). In Fig. 3.9 we show the average trajectory computed from 5000 different trajectories including the ones in Fig. 3.8 (blue line). In red we show the analytic average trajectory computed using the expressions in Eq. (3.5) and Eq. (3.6). We see that the numerical model reproduces the theoretical result deduced and that both recover the logarithmic spiral. This illustrates how, for long times, the swimmers behave diffusively, diffusing around the central

point

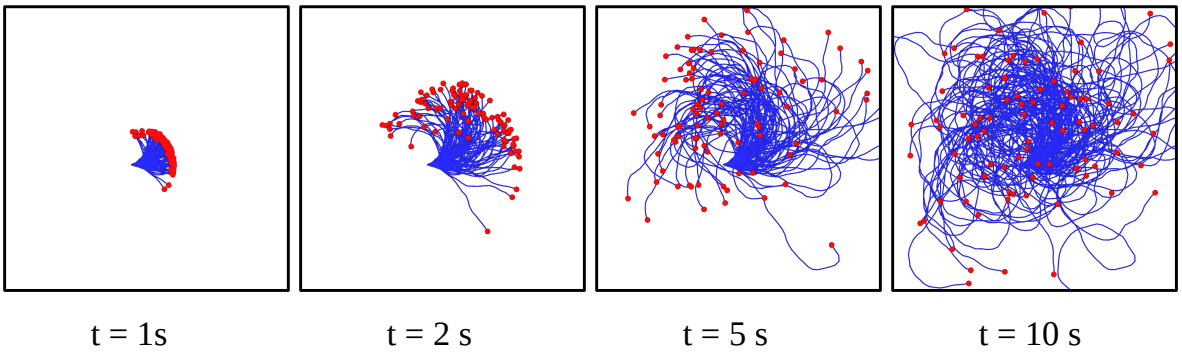

Figure 3.8: Snapshots of the trajectories of 100 chiral active particles with radius $r_0 = 1.5$ μm, $D_R = 0.8$ rad/s and $v = 10.95$ μm/s, with initial conditions $(x = 0, y = 0, \theta = 0)$ at different instants of time after being generated.

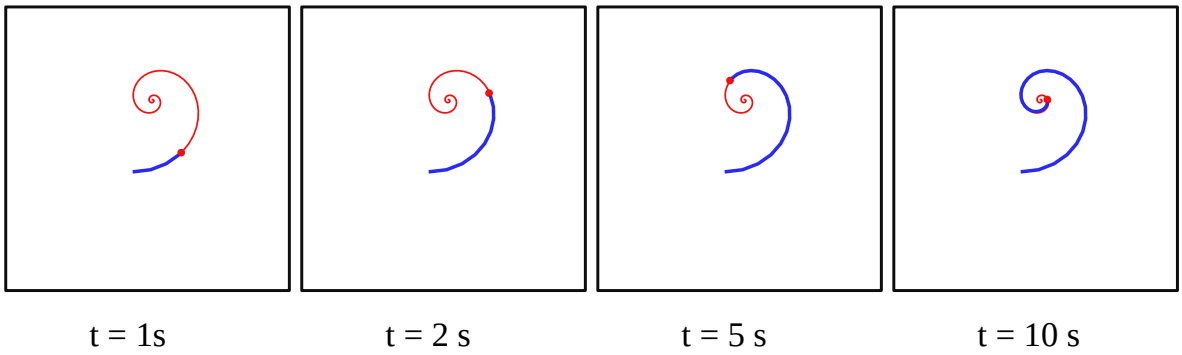

Figure 3.9: Average trajectory taken from of 5000 different trajectories of chiral active particles with radius $r_0 = 1.5\mu$m, $D_R = 0.8$ rad/s and $v = 10.95$ μ/s, with initial conditions $(x = 0, y = 0, \theta = 0)$ at different instants of time after being generated.

of the spiral. We compared also the mean squared displacement calculated analytically Eq. (3.11), with the ones measured in the simulations. The results are presented in figure 3.10 and show to be in good agreement.

3.3 Results

To completely identify what is the mechanism responsible for the non-monotonic behavior, we make use of the possibility of the numeric simulations to switch on and off each of the interactions with the obstacles (each of the three contributions). In Fig. 3.11, we present the comparison between the experimental and numerical results obtained for the effective distance L_{eff}, the effective velocity V_{eff} and the effective angle difference $\Delta\Theta_{\text{eff}}$.

Fig. 3.11a shows a good agreement between the experimental and simulated values while considering the three contributions (Repulsion+Forward-Scattering+Tumble-Collisions). In particular we observe the same non-monotonic behavior as in experiments with a slight increase of the peak (highest value) of the distributions of L_{eff} and V_{eff} and a much more accentuated decrease of values (after the peak) for the normalized effective velocity. It should be noticed how our model, which neglects the particle shape,

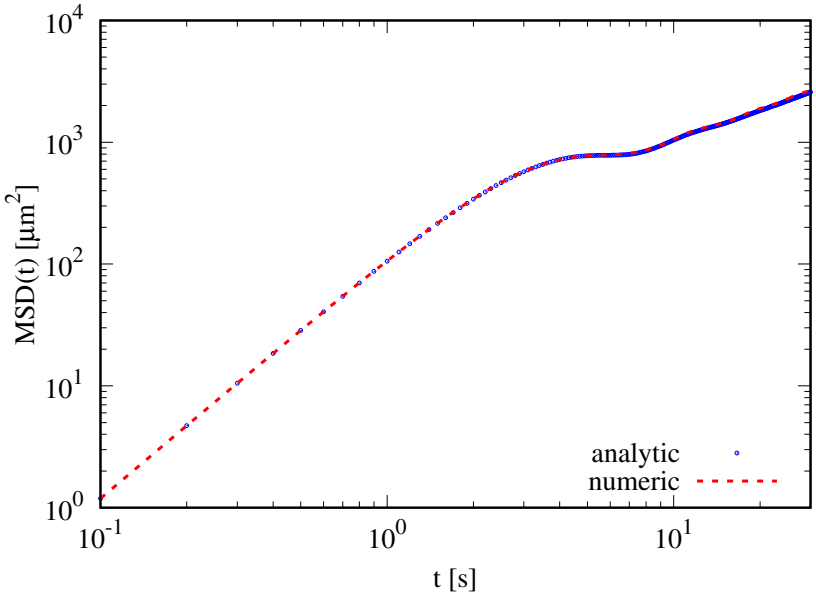

Figure 3.10: Red dashed line: Mean square displacement of 5000 different trajectories of chiral active particles, calculated numerically with $D_R = 0.8$ rad/s and $v = 10.95$ μm/s, with initial conditions $(x = 0, y = 0, \theta = 0)$. The blue dots correspond to mean square displacement calculated in the same conditions using Eq. (3.11).

specific mechanism of motion (run and tumbles), and that does not follow the precise distribution of obstacles of experiments, is able to closely reproduce qualitatively as well as quantitatively the observed experimental behavior.

In Fig. 3.11b we show the same comparison with experiment but now neglecting the tumble-collisions type of interaction with obstacles (R+FS). We see that even tough the results are quantitatively different from those considering all contributions, the same qualitative behavior is observed, namely the initial increase of the values of L_{eff} and V_{eff}, and a monotonically decrease for high values of ρ.

As for the model excluding both the scattering interactions and the tumble-collisions, maintaining only the repulsive force 3.11C, we see a monotonic decrease for both the effective distance and normalized effective velocity and a monotonic increase for the effective angle difference as expected. These numerical results, therefore, show how forward-scattering is the primary mechanism of particle-obstacle interaction behind the non-monotonic trends of L_{eff} and V_{eff} with increasing ρ, with tumble-collisions mainly influencing this behavior quantitatively rather than qualitatively. Without this mechanism, L_{eff} and V_{eff} decrease monotonically with the density of obstacles as the particles get increasingly reflected backward by their presence due to the repulsion term (Fig. 3.11c and Fig. 3.12c).

The rectification of the bacteria trajectory due to local forward-scattering interactions is also evidenced by looking at the angle difference distributions for different number of obstacles, Fig. 3.12. The main model (R+FS+TC), follows the experimental distributions very close, having an increase of the probability of higher values at $\rho = 2\%$ obstacle concentration and increase of the probability of trajectories that turn back once again at around 10 $\%$ obstacle concentration.

To test the robustness of these results, we repeated the same simulations (for the complete model) for different obstacle distributions, in particular, beads arranged according to a triangular lattice and through a random distribution of non-overlapping trimers. The main conclusion that we can take out of these results is the fact that the enhancement caused by a relatively low density of obstacles is robust and is not (at least qualitatively) dependent on the type of the obstacle distributions since it is observed, both for larger clusters (trimers) of beads deposited randomly without overlapping, but also for highly

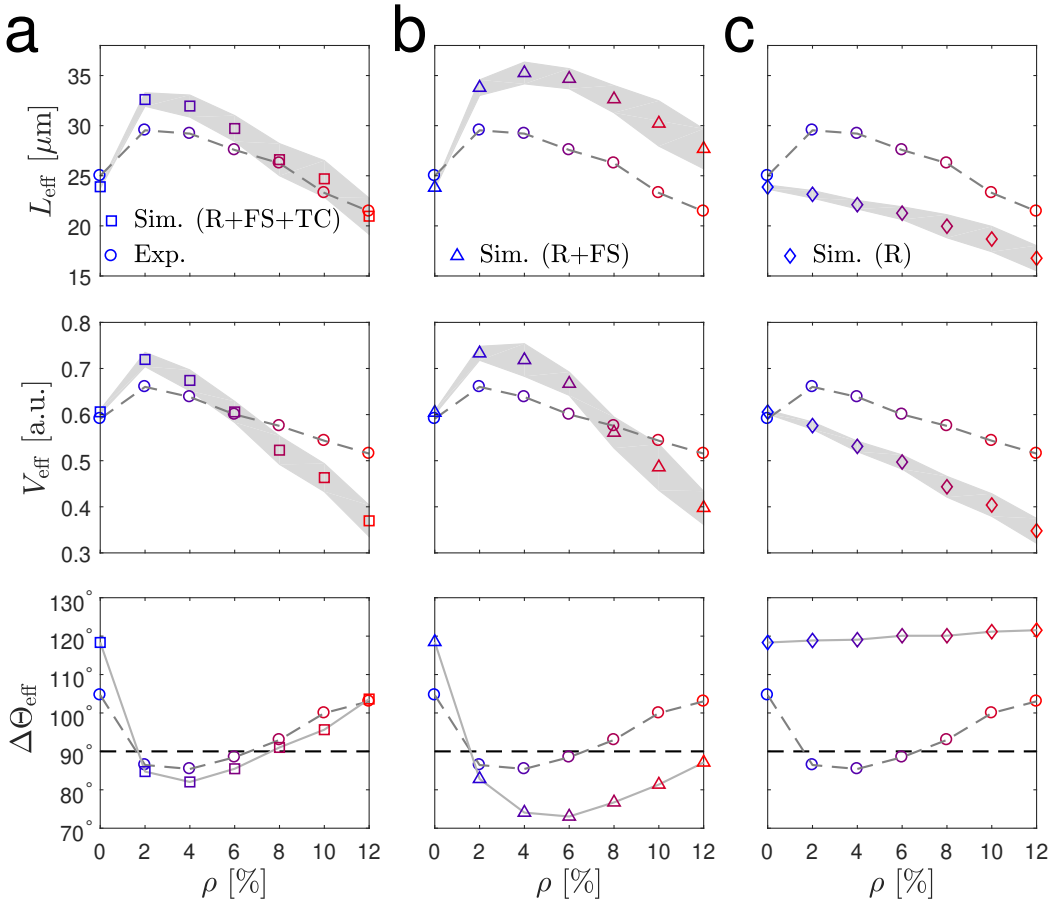

Figure 3.11: (a-c) Simulated average effective propagation distance L_{eff} , normalized average effective propagation speed V_{eff} and average change in effective propagation direction $\Delta\Theta_{\text{eff}}$ as a function of the obstacle density ρ for active chiral particles self-propelling through a circular area of radius $R = 25$ μm containing obstacles distributed at random without overlap in the presence of (a) all three cell-obstacle interaction terms (R: repulsive interaction; FS: forward-scattering; TC: tumble- collisions), (b) without tumble-collisions (TC) and (c) with repulsion (R) alone. Each value is obtained from averaging over 3000 different trajectories. The corresponding probability distributions of the change in effective propagation direction are shown in Fig3.12. The corresponding experimental values are shown for reference (circles).

spatially space-correlated beads, in a triangular lattice. However, as expected, the corridors formed in a periodic lattice, allow a better proliferation of the organisms, decreasing the number of head on collisions and consequently increasing the values of V_{eff} and L_{eff}, for high obstacle densities, while deceasing the average values of the angle difference.

Fig. 3.14 shows how the measured curves scale with the increase of the radius of the circular region of analysis both for experiments and simulations. Once again is possible to verify the agreement between experiments and simulations. It is interesting to notice how the enhancement of proliferation for low obstacle density, is preserved even for higher sizes as is possible to see for $R = 50$ μm.

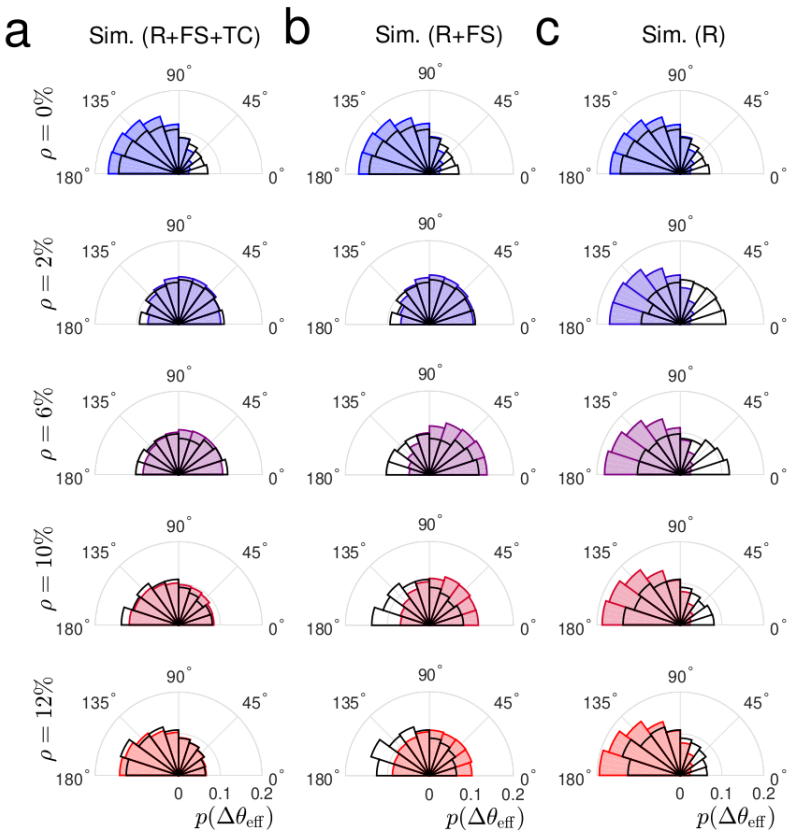

Figure 3.12: Simulated change in effective propagation direction for active chiral particles in the presence of uniformly distributed micro-obstacles

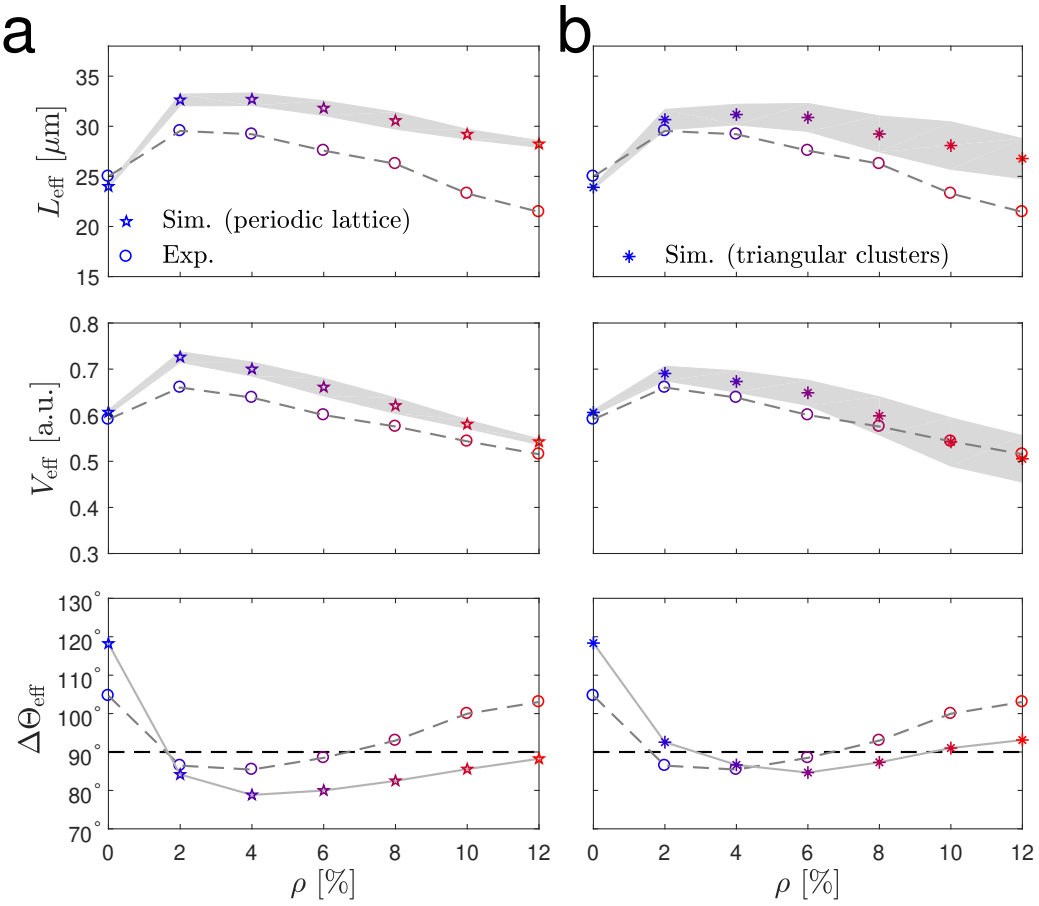

Figure 3.13: Comparison between experiments and numerical simulations: influence of obstacle distribution. (a-b) Simulated average effective propagation distance L_{eff}, normalized average effective propagation speed V_{eff} and average change in effective propagation direction $\Delta\Theta_{\text{eff}}$ as a function of the obstacle density ρ for chiral active particles self-propelling through a circular area of radius $R = 25\mu$m containing obstacles distributed according to a triangular periodic lattice (a) (Fig. 3.7b) and a random distribution of non-overlapping trimers (b) (Fig. 3.7c). The interactions with the obstacles include all three cell–obstacle interaction terms: repulsive interactions, forward-scattering events and tumble-collisions (Methods). Each value is obtained from averaging over 3000 different trajectories. The shaded area around the average values of L_{eff} and V_{eff} represents one standard deviation. The solid line connecting the values of $\Delta\Theta_{\text{eff}}$ is a guide for the eyes. The corresponding probability distributions of the change in effective propagation direction $\Delta\Theta_{\text{eff}}$ are shown in Fig 3.14. The corresponding experimental values are shown for reference (circles)

.

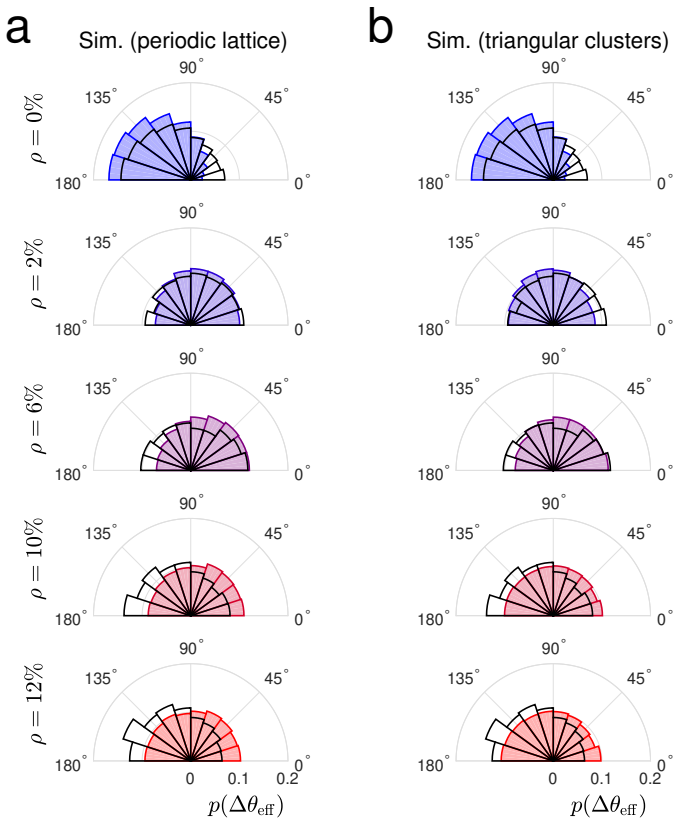

Figure 3.14: Simulated change in effective propagation direction for active chiral particles in the presence of micro-obstacles with different distributions. The dependence on L_{eff}, V_{eff} and $\Delta\Theta_{\text{eff}}$ is shown in Fig. 3.13.

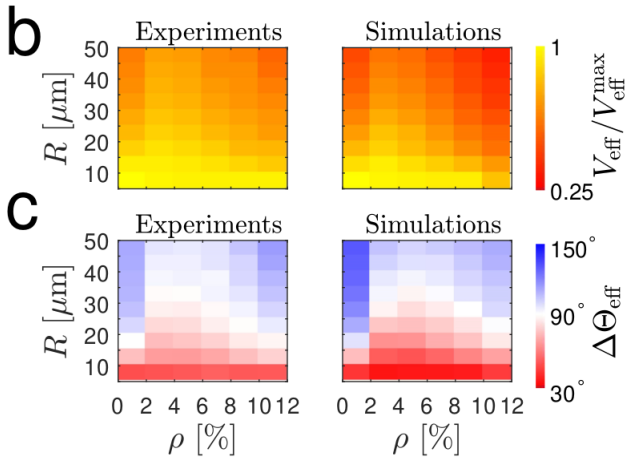

Figure 3.15: Scaling behavior of chirality rectification in space. (a) Experimental average effective propagation speed L_{eff} as a function of the obstacle density ρ for circular areas of increasing radius R. Each value is obtained from averaging over at least 200 different trajectories. The shaded areas around the average values represent one standard deviation. The case for R = 25 μm, Fig .3.3 is also shown for reference. (b) Average effective propagation speed V_{eff} and (c) average change in effective propagation direction $\Delta\Theta_{\text{eff}}$ as a function of ρ and R in experiments and simulations. Veff is normalized to its maximum values V_{Max} eff for visualization purposes ($V_{\text{eff}}^{\text{Max}} = 0.79$ in experiments and $V_{\text{eff}}^{\text{Max}} = 0.95$ in simulations).

Chapter 4

Space of parameters

One of the advantages of computer simulation is the possibility to explore the parameter space of our system in a systematic way. Thus it is possible to make a further theoretical study by testing cases whose experimental realization may not be possible or may be too demanding in terms of time and resources. In the particular case of the system under study, making an experimental study of all parameters means having complete control over the temperature of the system, the type of solvent, the distribution of obstacles in space, but more difficult, over the physical characteristics of the active particles, meaning to be able to vary the physical shape of bacteria and their interaction with obstacles.

In this section, we aim at performing such a systematic study. Having now a model that is able to reproduce the movement of chiral bacteria in a two dimensional bath of obstacles, we explore our model with the goal of making predictions about the individual behavior of chiral bacteria with different physical characteristics that translate into different values of the parameters adopted for the chiral constant Ω_0, for the typical distance of interaction with the obstacles r_1, for the constant of rotational diffusion D_R and for the average swimming velocity v.

To evaluate the dependence of the dynamics on each one of these parameters we made a systematic study in which each parameter is varied independently, keeping all the others constant, with values equal to the ones used to reproduce the experimental behavior in the previous chapter, unless stated otherwise.

First, we start by looking at how the system behaves in the absence of obstacles focusing on the dependence of the effective distance L_{eff} , the effective angle difference Θ_{eff} and the effective normalized velocity V_{eff}[1]. Next, we look at how the presence of obstacles changes the behavior of these quantities. We employ the same model presented in the previous chapter with the three contributions discussed (R+FS+TC). In the following, the conditions of the simulations are the same but the obstacles are randomly distributed over the whole simulation box and the time ran for each sample was increased from $300\ s$ to $500\ s$ and the number of samples (different obstacle configurations) to 100, for better statistics.

4.1 In the absence of obstacles

As explained in Chapter 3, the non-monotonic behavior observed in the three parameters measured can be explained by the change of the shape of the trajectories caused by the presence of the obstacles. The forward scattering interaction with the obstacles rectifies the typical circular trajectories of the chiral

[1] While for the previous chapter the measurements were made considering only the trajectories with penetration depth larger than 10% of the diameter of the area of analysis, in the following chapters all trajectories that enter the circle are considered.

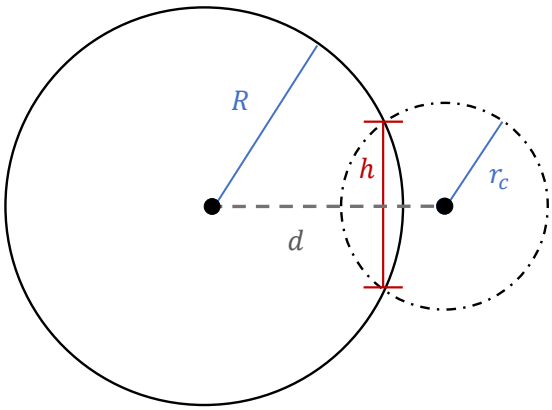

Figure 4.1: Scheme used for the calculation of the distance h between the two points where the circles intercept each other. This height corresponds to the effective distance l_{eff} a bacterium travels in a circle of radius R when moving in perfectly circular paths ($D_R = 0$) of radius r_c when the center of both circles are a distance d apart.

swimmers increasing the effective distance L_{eff} as well as V_{eff}. We now try to understand how L_{eff} depends on the control parameters.

We shall start with the simplest case, where $D_R = 0$. In limit, the trajectory of the bacteria is a circle of radius $r_c = \frac{v}{\Omega_0}$. If we fix the radius of the path, by fixing v and Ω_0, our system will consist of a series of circular paths at a distance d of the center of the circular region of analysis. The effective distance between the entrance and exiting point can then be obtained through the expression [39]

$$h = \frac{1}{d}\sqrt{(-d + r_c - R)(-d - r_c + R)(-d + r_c + R)(d + r_c + R)}, \tag{4.1}$$

which tells us the "height" of the lens formed by the intersection of the two circles, Fig.4.1.

The trajectories used to calculate the average of the effective distances are those that intersect the circle of analysis, thus d can vary between $|R - r_c|$ and $R + r_c$. Since the probability of having the center of the trajectory at a given distance of the simulation box should be uniform, the probability distribution of d, $P(d)$, can be assumed to be

$$P(d) = \frac{2\pi d}{\pi\Big[(R + r_c)^2 - (R - r_c)^2\Big]}. \tag{4.2}$$

The average effective distance L_{eff} will then be given by

$$L_{\text{eff}} = \int_{|R-r_c|}^{R+r_c} h(R, r_c, d')P(d')dd'. \tag{4.3}$$

Solving the integral numerically[2], we obtained the solid line in Fig.4.2. In the same figure, we can compare the results obtained by our numerical model for different values of the rotational diffusion constant, namely $D_R = 0.0075, 0.075, 0.225$ rad^2/s. It can be observed that, as expected, for low values of D_R the numerical model and the analytical approximation match. For high values, such as the one used in the previous chapter we observe a good match for low values of r_c. However, for values of $r_c > 15$ μm, the numerical curve goes considerably below the analytic one.

The rotational diffusion performed by the bacteria for trajectories with typical radius of curvature significantly higher than $R = 25$ μm reduces the typical size of the trajectories of the bacteria inside the

[2]For simplicity we solved the integral using *Mathematica 11*.

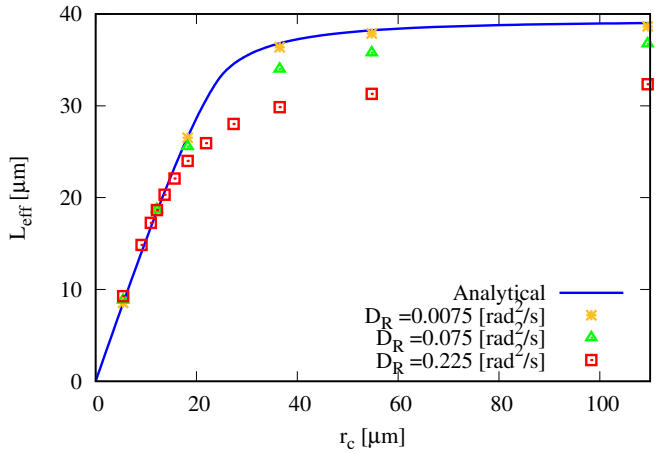

Figure 4.2: Average effective propagation distance L_{eff} as a function of the typical radius of curvature $r_c = \frac{v}{\Omega_0}$ for a circular area of radius $R = 25$ μm. r_c is varied by varying Ω_0 keeping $v = 10.95$ μ m/s Each value is obtained from averaging 10000 different trajectories. The blue line corresponds to the analytic values for $D_R = 0$. The yellow, green and red dots correspond to the numerical results for different values of D_R (as described in the figure).

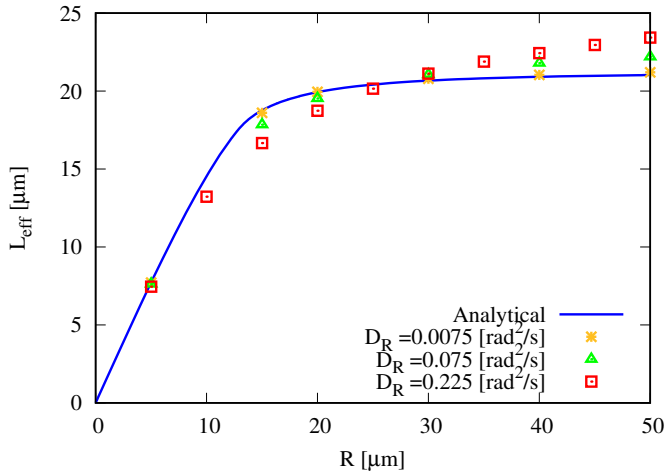

Figure 4.3: Average effective propagation distance L_{eff} as a function of the radius of the circular analysis area R for a typical radius of curvature $r_c = 13.51$ μ m. r_c is kept constant by $\Omega_0 = 0.8$ rad/s and $v = 10.95$ μ m/s Each value is obtained from averaging over 10000 different trajectories. The blue line corresponds to the analytic values for $D_R = 0$. The yellow, green and red dots correspond to the numerical results for different values of D_R (as described in the figure).

circle. More interestingly, by looking at how the analytical and numerical curves evolve as a function of the radius R, we see the opposite effect happening for high values of R, Fig.4.3. For values of R lower than 25 μm, the numerical lines for $D_R = 0.075, 0.225$ rad^2/s go below the analytic one but are above it for higher values. This means that the difference between the numeric results and the analytic model that considers no rotational diffusion changes with the length scale of the trajectories.

To understand the different behaviors one must notice that by varying R we are not only varying the area of the analysis region, but also the average time that the bacteria takes to perform the trajectory. Consequently, by varying the size of the circle, we are looking at the effective spread of bacteria at different time scales.

The effect of the angular noise at different time scales is illustrated in Fig.4.4. For early times, the bacteria moves ballistically, as discussed in Chapter 3, and the rotational diffusion leads to deviations from this motion. For larger time scales ($t >> \tau_R = D_R^{-1}$), the bacteria whose preferential direction of motion diffuses less will still be orbiting the same center of trajectory (or somewhere near it), while

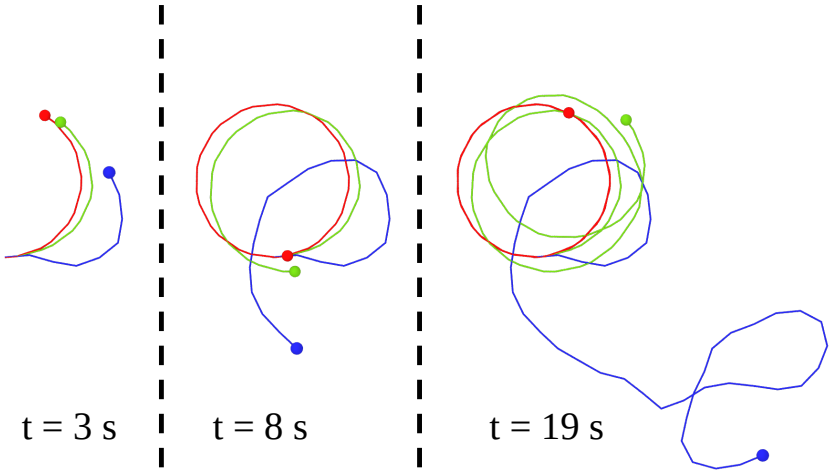

Figure 4.4: Snapshots of the motion of three active chiral particles (R+FS+TC) with $\Omega_0 = 0.8$ rad/s for three different values of the rotational diffusion constant, $D_R = 0.0075$ rad^2/s (red), $D_R = 0.075$ rad^2/s (green), , $D_R = 0.225$ rad^2/s (blue).

the bacteria with higher rotational diffusivity will tend to spread further away from this initial point. Smaller analysis circles will promote short trajectories thus close to the first type of behavior regarding the rotational diffusion constant while larger ones will promote larger trajectories thus, more affected by rotational diffusion. This interpretation is also corroborated by a more quantitative analysis based on the mean square displacement of the bacteria for different values of D_R, as shown in Fig.4.5.

The blue line corresponds to the deterministic case where $D_R = 0$, and shows an early ballistic regime and a periodic behavior for times larger than the period of the orbit. As already explained in a more illustrative fashion, and by looking at the inset of the figure it is possible to see that as D_R increases the bacteria get more and more localized and the MSD curves go below the "ideal" one. However, it is also noticed that for times $t < 4$ s the curve with highest value of D_R is also the one with higher MSD, since its rotational diffusivity will disrupt the periodic nature of the trajectory and allow the bacteria to proliferate more efficiently through space, thus corroborating our more intuitive interpretation.

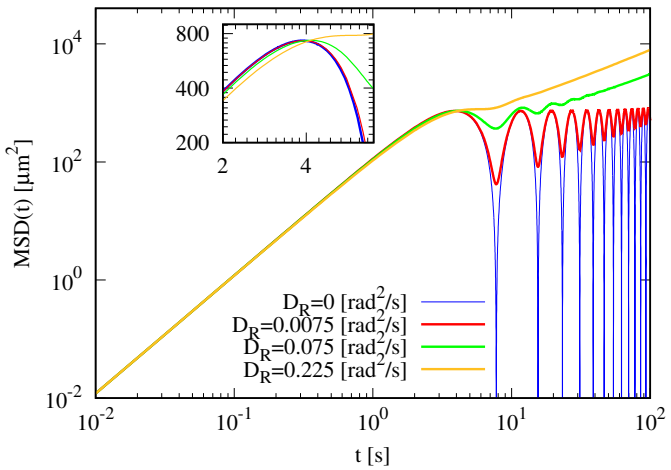

Figure 4.5: Mean square displacement calculated from Eq.2.19 for different values of the rotational diffusion constant D_R. The inset shows the time at which the lines cross, and the lines with $D_R > 0$ are above the one for $D_R = 0$.

The radius at which numeric curve for the the average effective propagation distance for $D_R = 0.225$ rad^2/s crosses the one for $D_R = 0$, is also consistent to the radius at which the average time a random walker with constant velocity spends inside the a circle. This time $\langle t \rangle = \frac{\pi R}{2v}$, deduced by Frangipane et al

[12], for conditions that match the ones in our system is about 3.6 s for a radius $R = 25$ μm and 4.3 s for a radius of $R = 30$ μm. These time intervals are also consistent with the time (about 4 seconds) at which the respective analytical MSD lines cross, that correspond to the radius intervals where the $D_R = 0$ and $D_R = 0.225$ rad^2/s lines for the average effective distance cross. From these arguments is then possible to explain the different behaviors that a bacteria with high rotational diffusion has relative to one that travels in perfect circles, and it is also possible to predict the time and length scale, at which the behavior changes from one type to another.

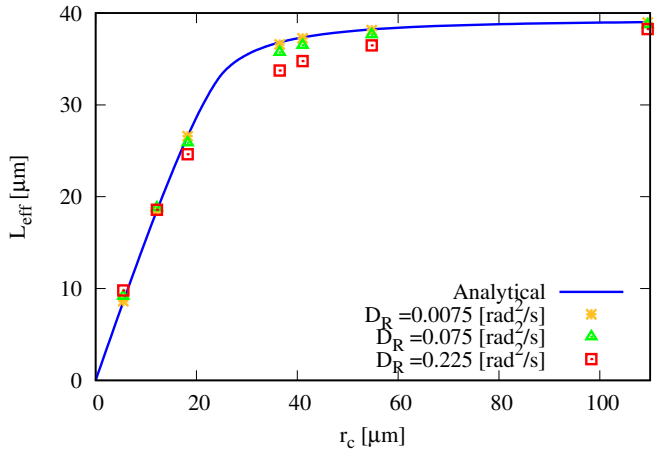

Figure 4.6: Average effective propagation distance L_{eff} as a function of the typical radius of curvature $r_c = \frac{v}{\Omega_0}$ for a circular area of radius $R = 25$ μm. r_c is varied by varying $v = 10.95$ μm/s keeping $\Omega_0 = 0.8$ rad/s. Each value is obtained from averaging 10000 different trajectories. The blue line corresponds to the analytical values for $D_R = 0$. The yellow, green and red dots correspond to the numerical results for different values of D_R.

Having looked at how the system responds to the change of the radius of the analysis region as well the change of the radius of curvature by changing the angular constant Ω_0, we should remember that there is another way to change the radius of curvature of the "ideal" trajectory, and that is by changing the typical velocity v of the bacteria. In Fig.4.6, we show how L_{eff} depends on the radius of curvature by varying it via the parameter v. In this figure we observe the same kind of dependence on the parameter D_R but a less accentuated decrease of L_{eff} with the increase of the rotational diffusivity. This change is less evident than the one observed in Fig.4.2 due to the fact that, by increasing the radius of curvature by the increase of v instead of the decrease of Ω_0, we are actually reducing the time it takes for the bacteria to go through the same circumference. Therefore, the probability that the trajectory is perturbed by a significant diffusion of the preferred direction of motion is reduced. Thus, we can conclude that there are two typical time scales that must be considered in order to determine the behavior of our system. We must consider the typical time it takes for the bacteria to perform a complete "circle", that is set by $T = \frac{2\pi}{\Omega_0}$, and the typical time it takes for the bacteria to change this "circular" behavior due to the rotational diffusion and that is set by $\tau_R = D_R^{-1}$.

The behavior of the two remaining measurements will also be a consequence of the interplay between these time scales. For the average effective angle difference, we observe decrease for increasing values of r_c (Fig.4.7a), since increasing the typical radius of curvature of the trajectories will reduce the number of trajectories that "turn back" exiting near the entrance point. We also observe once again, that when we increase the radius of curvature by the increasing the velocity of the active particles, the curves for high D_R values are much closer to the ones low D_R, Fig.(4.7b). Lastly, we see that the effective angle difference tends to increase as we increase the circular area. This is as consequence of the the increase

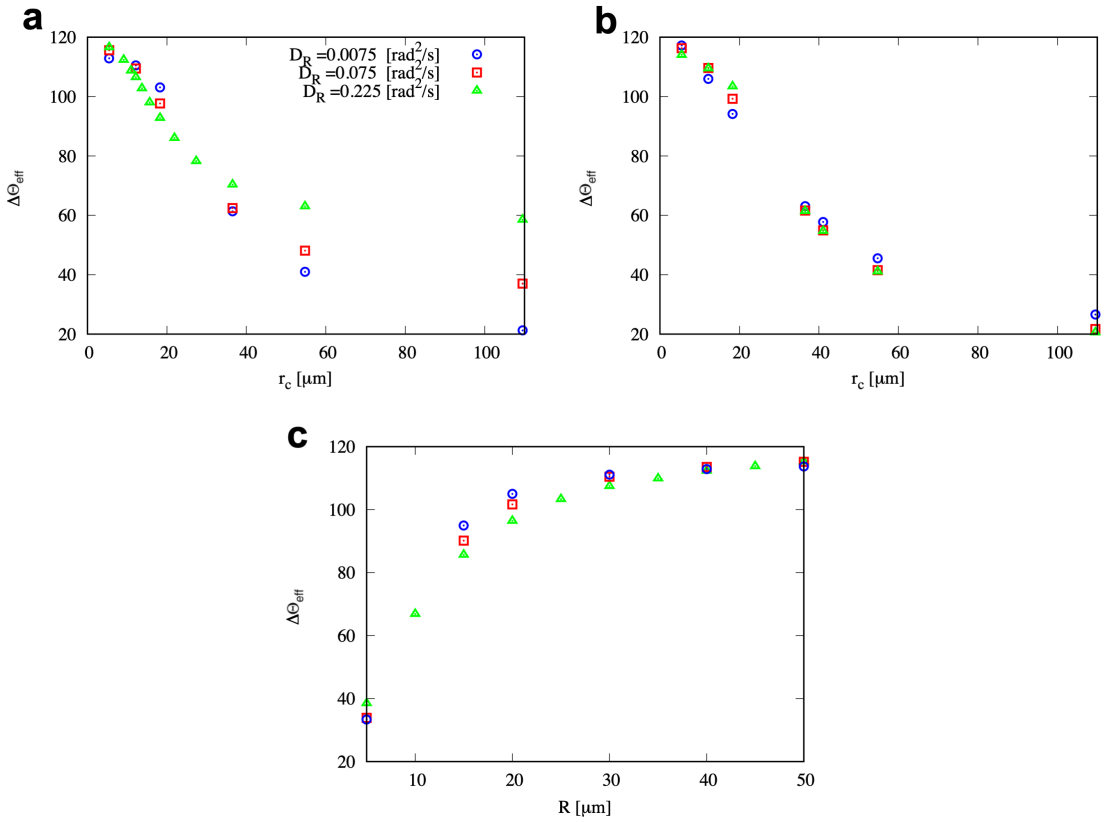

Figure 4.7: Average effective angle difference as $\Delta\Theta_{\text{eff}}$ a function of:(a) radius of curvature by changing Ω_0. (b) radius of curvature by changing v. (c) Radius of circular region of analysis.

of the probability that the trajectories have performed several “turns” before exiting the circle.

As for the average effective velocity, we see the increase when increasing the radius of curvature caused by the rectification of the trajectories, and a decrease with the size of the area of analysis as this effect gets lost with the size of the circle as observed also for L_{eff} and $\Delta\Theta_{\text{eff}}$.

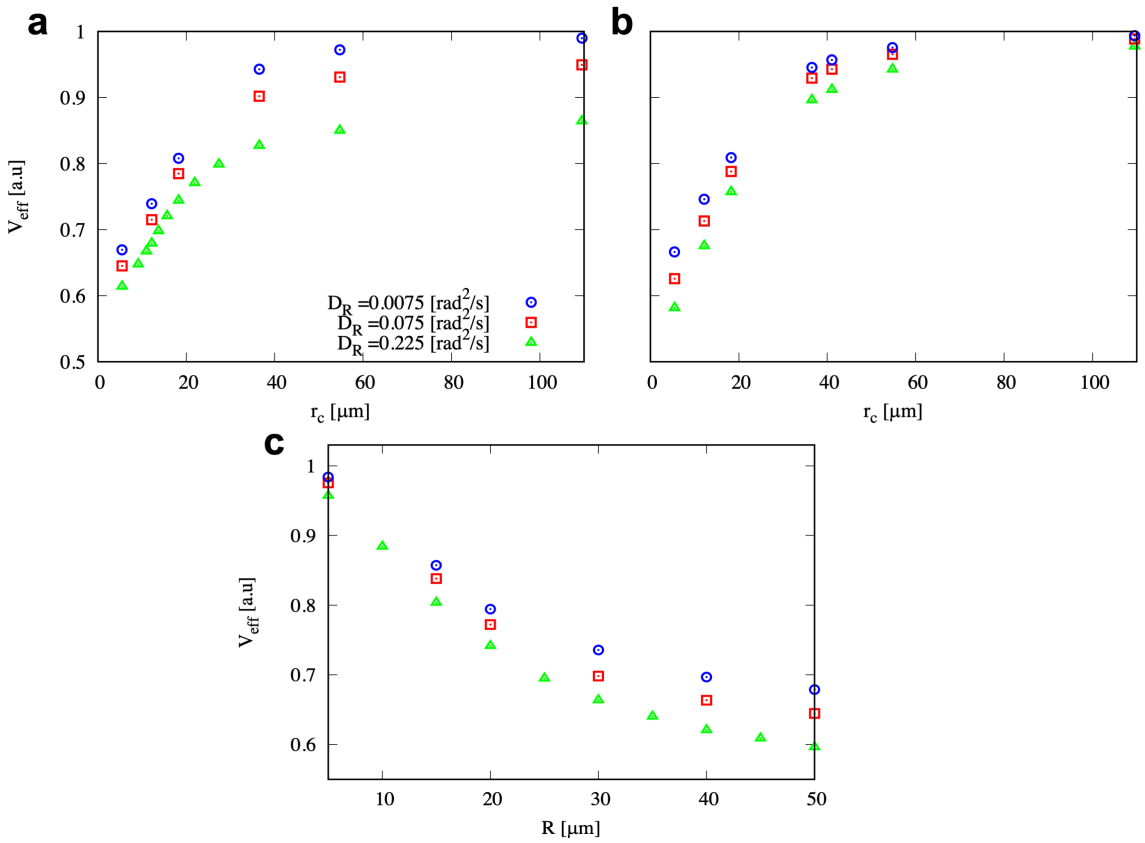

Figure 4.8: Average effective velocity difference V_{eff} as a function of:(a) radius of curvature by changing Ω_0. (b) radius of curvature by changing v. (c) Radius of circular region of analysis.

4.2 With obstacles

To determine what is the effect of the obstacles in the dynamics, we performed the same study as in the case with no obstacles for different obstacle concentrations ρ. For this, we changed the typical radius of curvature r_c by changing the value of Ω_0 with the linear velocity fixed at $v = 10.95$ μm/s. The results are presented in Fig.4.9. We see that for low obstacle densities (around $\rho = 2\%$) the propagation is increased as long as the radius of the trajectories is kept with values lower or of the same order of R. When r_c starts to be much higher than R the trajectories start to be similar to the ones of non-chiral swimmers (dashed lines) and the gain of the distance traveled due to the forward scattering interactions with the obstacles is lost. By increasing the number of obstacles, and for densities of $\rho = 6\%$ or higher, the typical length traveled before colliding with an obstacle is shorter than the typical length needed to notice the effect of the swimmers chirality and swimmers behave as non-chiral active particles colliding with multiple obstacles.

In Fig.4.10 we confirm that the non-monotonic behavior arises only when r_c is of the order of R or lower, since the curve obtained for $r_c = 53.75$ μm is monotonically decreasing with the number of obstacles. We also confirm by noticing that for values of $\rho < 6\%$ all the curves collapse, that the effect of chirality is lost.

By looking at how the average effective distance changes as a function of D_R in the presence of obstacles (Fig.4.11), we see that the monotonic decrease is maintained, becoming even more visible as soon as some obstacles are added to the environment.

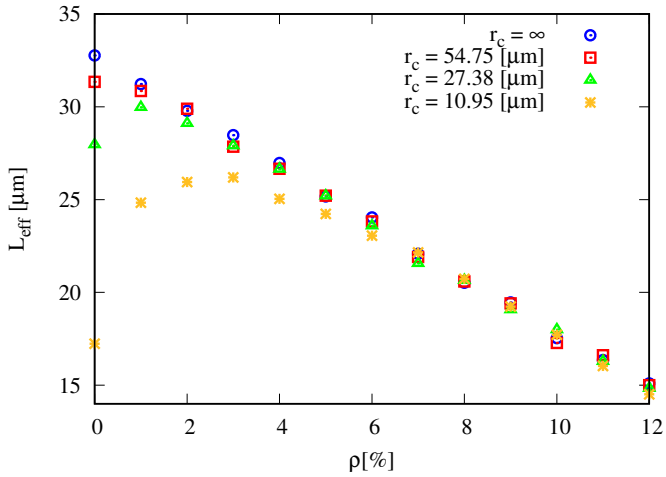

Figure 4.9: Average effective propagation distance L_{eff} as a function of the typical radius of curvature $r_c = \frac{v}{\Omega_0}$ for a circular area of radius $R = 25$ μm. r_c is varied by varying Ω_0 keeping $v = 10.95$ μm/s Each value is obtained from averaging 1000 different trajectories. The blue line corresponds to the analytical values for $D_R = 0$. The yellow, green and red dots correspond to the numerical results for different values of D_R.

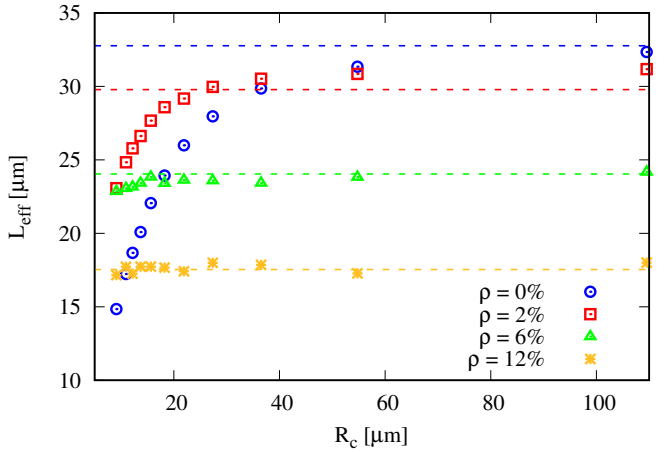

Figure 4.10: Average effective distance L_{eff} as a function of obstacle density ρ. Each line corresponds to a different radius of curvature for fixed $v = 10.95$ μm ,$R = 25$ μm, $r1 = 10.7$ μm.

As for how L_{eff} changes with the typical length of the forward scattering interaction (r_1), we see for low obstacle densities ($\rho = 2\%$) a similar dependence as for the for the radius of curvature, suggesting that, by increasing the length of interaction, we are in fact increasing the effective typical radius of curvature of the trajectories of the chiral swimmers. We also observe once more that, by increasing the density of obstacles (to $\rho = 6\%$), the dependence on r_1 starts to be negligible, since the chirality of the active particles starts to be irrelevant to the motion. For $\rho = 12\%$ the bacteria starts to behave once more like non-chiral active particles.

To conclude this analysis, we looked at the mean squared displacement obtained in the simulations for different concentration of obstacles ($\rho = 0, 2, 6, 12\%$), as shown in Fig.4.13. We confirm once more the enhancement in the proliferation of bacteria for $\rho = 2, 6\%$ relative to the homogeneous case ($\rho = 0\%$). However, we see once again (this time for different obstacle concentrations), that the system shows different behaviors at different time scales. While for times shorter than 6 seconds (as the average residence time of the trajectories in a circular area of radius R=25 μm), the bacteria will propagate more in an homogeneous environment than in one in with $\rho = 12\%$, for times larger that these, the behavior

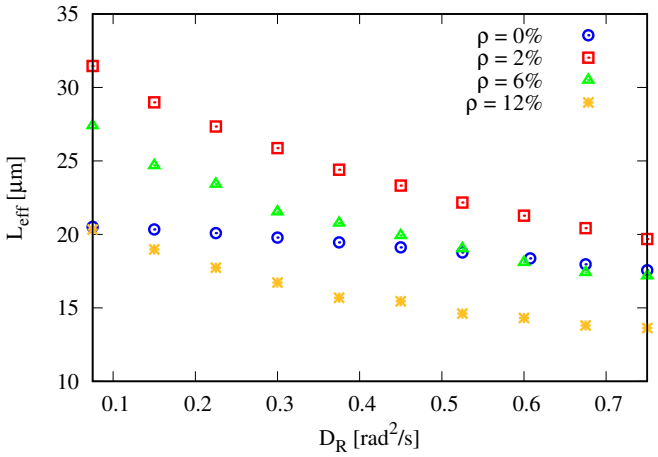

Figure 4.11: Average effective propagation distance L_{eff} as a function of the typical radius of the rotational diffusion constant D_R, for a circular area of radius $R = 25\mu$m, $\Omega_0 = 0.8$ rad/s and $v = 10.95$ μm/s. Each value is obtained from averaging 10000 different trajectories..

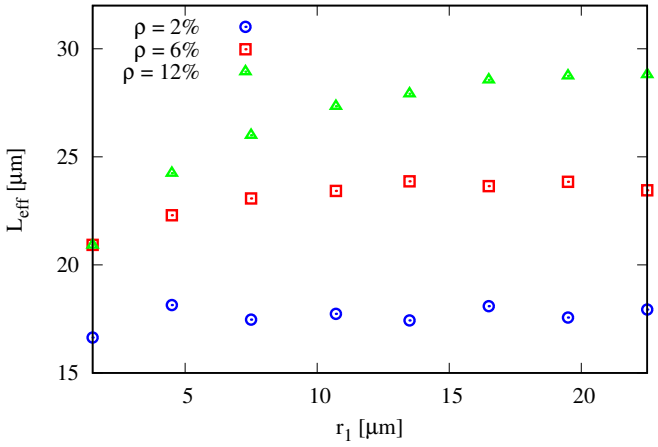

Figure 4.12: Average effective propagation distance L_{eff} as a function of the constant that set the typical length of the interaction r_1, for a circular area of radius $R = 25$ μm, $\Omega_0 = 0.8$ rad/s, $v = 10.95$ μm/s and $D_R = 0.225$ rad^2/s. Each value is obtained from averaging 10000 different trajectories.

is changed and the bacteria gets more localized in the absence obstacles than it is in a medium with high obstacle concentration. These results suggest that the enhancement in the mobility of chiral organisms might even be observed for high obstacle concentrations when large time scales are considered.

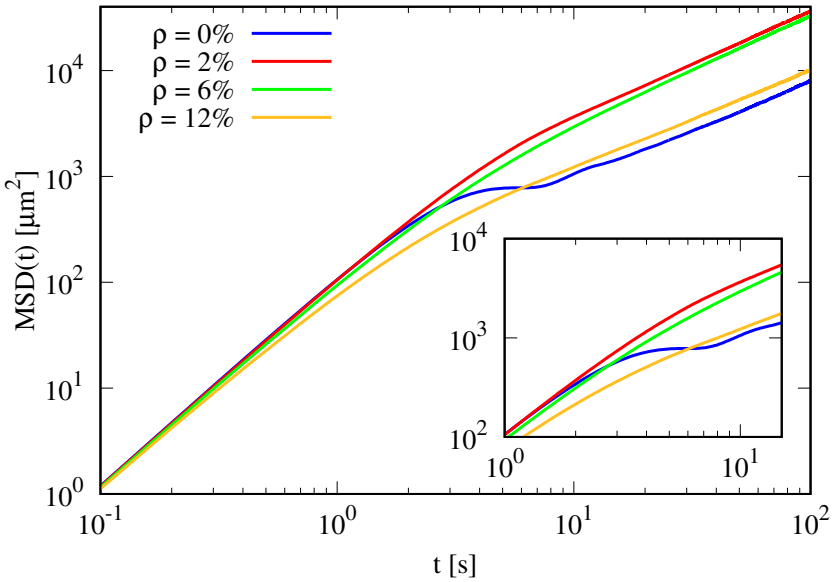

Figure 4.13: MSD as a function of time $\Omega_0 = 0.8$ rad/s, $v = 10.95$ μm/s and $D_R = 0.225$ rad^2/s, considering different obstacle concentrations. Each value is obtained from averaging 10000 different trajectories.

Chapter 5

Invariant properties of active random walks

Another interesting property of active Brownian particles and random walkers is the invariance of the average path length of trajectories (from entry to exit point of a given surface) to changes in the velocity or diffusion constants of the walkers . This was first shown in 2003 by Blanco and Fournier [6]. In their work they show how the specific characteristics that typically define a random walk, such as diffusion constants for translation and rotation, do not affect the average path length of the sub-trajectory inside a circle. They confirmed this numerically using Monte-Carlo simulations and from an analytic derivation assuming that a circle of radius R is drawn in a plain surface and that the distribution of velocities is isotropic. The average path length of any random walker inside a surface in two dimensions is then $\langle p \rangle = \pi \frac{S}{P}$, where S is the surface considered and P its perimeter. The authors explain this phenomenon by noting that if there is a decrease in the mean free path length of a walker (for example by increasing D_R), there will be an increase in the average mean path length of a large trajectory. However, the number of short trajectories will also be increased since the probability to leave the surface near the entry point will be higher.

More recently, it has been shown experimentally for non-chiral bacteria by Frangipane et al. [12], that this result can be generalized for the mean-residence time (average duration of the trajectories inside the circle). Assuming non-interacting random walkers moving with constant speed v and isotropic reorientation dynamics, the authors analytically derive the expression $\langle p \rangle = v\tau = \pi \frac{S}{P}$. More interestingly, this result is still verified in an environment filled with obstacles as long as "their presence does not significantly perturb the homogeneity of the density field in the accessible space and the isotropy of random walks along the domain boundary". In other words, if the interactions with the obstacles are just excluded volume, and no localization effects are verified, the expression can be adjusted just by taking into account the real space that can be occupied by bacteria, i.e, the total space minus the space occupied by the obstacles. Thus,

$$\langle t \rangle = \pi \frac{S}{Pv} \left(1 - \frac{Ns}{S} \right), \tag{5.1}$$

and,

$$\langle p \rangle = \pi \frac{S}{P} \left(1 - \frac{Ns}{S} \right). \tag{5.2}$$

To recover this result numerically, we start by building a model similar to the ones mentioned earlier

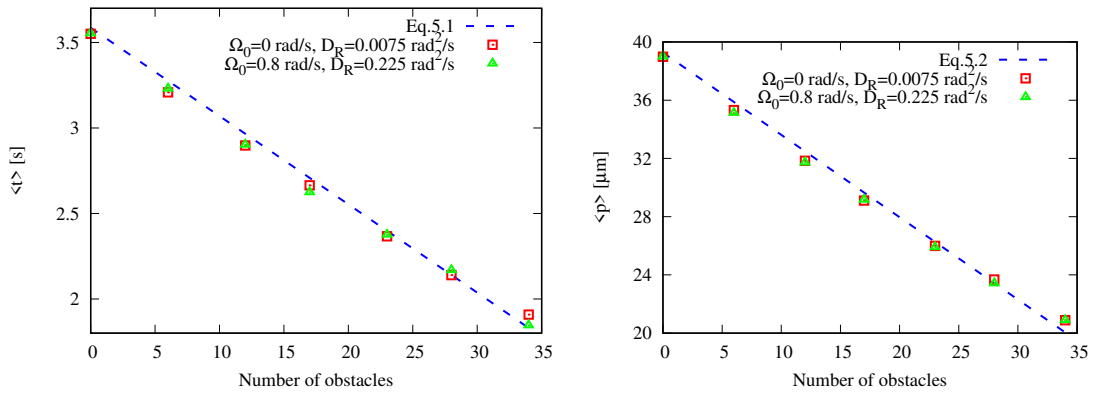

Figure 5.1: Comparison between the numerical Instant Tumble model (IT) for different values of D_R and Ω_0, and the analytical expressions of the average residence time (left) and average path length (right).

but where each swimmer interacts with the obstacles just by changing its direction of motion to the direction defined by the vector that goes from the center of the obstacle to the center of the active particle, any time the swimmer is at a distance $r < d$ to the closest obstacle (Instant Tumbles). The direction of motion is then instantaneously changed pointing in the direction opposite to the obstacle. We place the obstacles inside a circle of radius $R = 25$ μm. For simplicity, we obtained the trajectories of each active particle by using a first order method (Euler), integrating at each time step the equations:

$$\vec{r}_i(t) = \vec{r}_i(t) + \vec{f}_i\left(\vec{r}_i(t)\right)\frac{\Delta t}{\gamma} + v\vec{u'} \tag{5.3}$$

$$\phi_i(t) = \phi_i(t) + \Omega\left(\vec{r}_i(t)\right)\frac{\Delta t}{\gamma} + \xi_\phi \tag{5.4}$$

The results obtained are presented in Fig.5.1. We see that our model closely matches the equations Eq. 5.1 and the Eq. 5.2. It is also observed that both the mean residence time as well as the average path length are independent of the parameters Ω_0 and D_R since a similar result is obtained when considering $\Omega_0 = 0.8$ rad/s and $D_R = 0.225$ rad^2/s for the same values of v and R.

By looking at the distribution of path lengths for the case where $D_R = 0.0075$ rad^2/s and $\Omega_0 = 0$ (Fig.5.2), we observe that in the absence of obstacles there is a peak at the value $p = 2R$, in agreement with the chord-length distribution of a circle $P(p) = \frac{p}{2R\sqrt{4R^2-L^2}}$ that diverges near this value [12]. As the number of obstacles is increased, the probability to leave near the entry point is also increased, due to the possibility of being back scattered near the circle perimeter. However, the multiple collisions with obstacles will also increase the maximum path length. This way, in a similar line of reasoning as mentioned earlier, the augment in short trajectories is compensated by the emergence of trajectories with path lengths much larger than $2R$. In the case where $D_R = 0.225$ rad^2/s and $\Omega_0 = 0.8$ rad/s, it is possible to observe the same kind of compensation between short and large trajectories even though the presence of chirality and the increased rotational diffusion changes the shape of the distribution.

However, for the models considered in Chapter 3 (R+FS and R+FS+TC), we see that the mean residence time increases with the number of obstacles (Fig.5.3). In both situations the interaction the organisms establish with the obstacles are such that every time a swimmer is blocked by one or more obstacles, it has to wait a certain time until its direction changes, due to the rotational diffusion or to efficient tumble collisions (in the case R+FS+TC). Since the waiting time after a bacteria gets blocked will depend on both cases on the typical time it takes for it to change direction (D_R^{-1}), this invariant property is broken. Interestingly, the same effect can be observed for the average length traveled. By

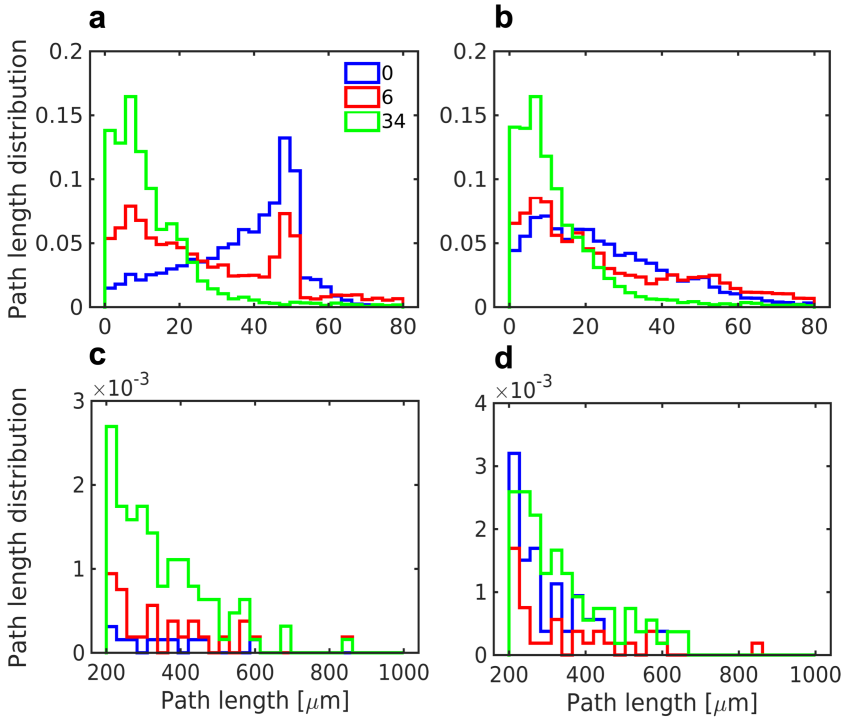

Figure 5.2: Distribution of path lengths in the IT model for: (a) $D_R = 0.0075$ rad^2/s and $\Omega_0 = 0$ and (b) $D_R = 0.225$ rad^2/s and $\Omega_0 = 0.8$ rad/s. (c) and (d) show respectively to the same distributions as in (a) and (b) for higher values of the path length.

adding a resting time upon collision, the property that makes that the increase in the average path length due to multiple scatterings is compensated by an increase in the number of short trajectories is no longer valid. This way, the mean path length will no longer be invariant to parameters that influence this "resting time" such has the constant of rotational diffusion in our models. This phenomenon is explained by the fact that, in a system where the organisms get "stuck" for some time after colliding, the bacteria will spend more time performing large trajectories and will not be available to enter and leave the sufficient number of times to increase the number of short trajectories that would compensate the larger ones. In other words, when there is some resting time upon collision, the relative frequency of the larger trajectories is increased and the relative frequency of shorter trajectories decreased (Fig.5.4).

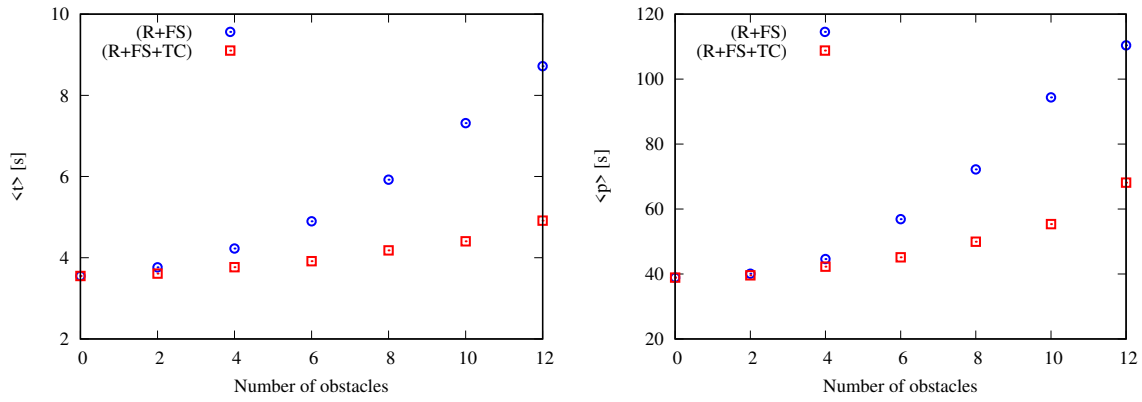

Figure 5.3: Mean residence time and average path length as a function of the number of obstacles for the models (R+FS) and (R+FS+TC).

We may conclude that for both models, by increasing the number of obstacles, the bacteria get more

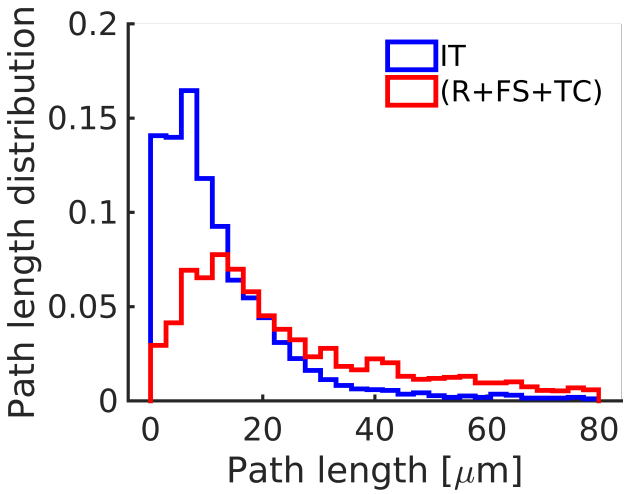

Figure 5.4: Comparison between the distributions of path lenghts for $\rho = 12\%$ for the IT model and the (R+FS+TC) both using $\Omega_0 = 0.8$ rad/s, $D_R = 0.225$ rad^2/s and $R = 25$ μm.

localized near these, and the uniformity condition is broken thus breaking the invariant properties of $\langle t \rangle$ and $\langle p \rangle$.

Chapter 6

Conclusion

We presented the experimental results from the group of Dr. Giorgio Volpe from the Univeristy College of London that show that a relatively low density of obstacles increases the proliferation of peritrichously flagellated bacteria. We propose a numerical model based on chiral active Brownian particles cruising through random obstacles that corroborates the universality of the experimentally observed behavior.

The model highlights how the interaction with a few obstacles enhances particle's propagation on surfaces as long as two main ingredients are present: chirality in the particle's motion and a rectification of the chiral motion during the repulsive interaction with the obstacles. Overall, our numerical results suggest that the experimentally observed behavior should be independent, at least qualitatively, of the microscopic nature of the self-propulsion mechanism and of the repulsive interaction between particles and obstacles as long as the two previous conditions are satisfied. Undoubtedly, further surface motility experiments are required to understand to which extent these two conditions apply to other bacterial swimming mechanisms other than the run-and-tumble of peritrichously flagellated *E. coli* cells as well as to test how the qualitative and quantitative nature of the cell-obstacle interaction changes with the swimming mechanism and the mechanism used by the cells to change direction of motion. When tumble-collisions are included, our simplified model with spherical particles can reproduce the main experimental observations obtained with *E. coli* cells in a close-to-quantitative fashion. In principle, the quantitative match between our experimental observations and numerical results can be improved further by taking into account the actual cell's shape and exact swimming mechanism.

We exploited how each control parameter of our model influences the dynamics of chiral bacteria. By developing an analytic model, where circular periodic trajectories are considered, we show that one of the relevant parameters to characterize the behavior of chiral organisms is the typical curvature radius (set by the ratio between the linear and angular velocities). In general the parameters that characterize the effective propagation of bacteria in flat homogeneous surfaces have a dependence on this typical radius of curvature similiar to the one found in the analytic study of circular trajactories. We show that both match in the absence of obstacles in the limit where there is no rotational diffusion. We show that as the rotational diffusion coefficient increases, the trajectories tend to get more localized for time scales shorter than the period of the corresponding circular orbit. For larger time scales, increasing the rotational diffusion coefficient enhances the difusion of the bacteria. As for the presence of obstacles, we show that the overall dependence on each of the previous parameters is mantained but that the presence of some obstacles enhances the motility of the chiral organisms as long as the typical radius of curvatures considered are shorter or about the same size of the length of the trajectories observed.

We also have shown that the mean path length and mean residence time of the trajectories is not

always invariant as previously reported for random walkers interacting repulsively with obstacles. Although they are invariant for simple chiral swimmers they are not when the obstacle/bacteria interactions break the homogeneity of the density field. In the future, we aim at characterizing how this obstacle-induced localization depends on the velocity and diffusion coefficients and at finding the analytical expressions that describe the dependence of the mean residence time and mean path length of the trajectories of active particles in these conditions. Knowing how these measurements depend on the physical characteristics of the organisms and on the interactions between them and the obstacles can help to improve the characterization of the the properties of the medium, the particle/obstacle interactions or the main features of the active particle motion in real contexts.

Bibliography

[1] C. Bechinger, R. Di Leonardo, H. Löwen, C. Reichhardt, G. Volpe, and G. Volpe. Active particles in complex and crowded environments. *Reviews of Modern Physics*, 88, 2016.

[2] H. C. Berg and R. M. Berry. *E. Coli in motion*, volume 58. 2005.

[3] C. Berne, C. K. Ellison, A. Ducret, and Y. V. Brun. Bacterial adhesion at the single-cell level. *Nature Reviews Microbiology*, 16:616–627, 2018.

[4] X. Bian, C. Kim, and G. E. Karniadakis. 111 years of Brownian motion. *Soft Matter*, 12:6331–6346, 2016.

[5] F. Black and M. Scholes. The pricing of options and corporate liabilities. *Journal of Political Economy*, 81:637–657, 1973.

[6] S. Blanco and R. Fournier. An invariance property of diffusive random walks. *Europhys. Lett*, 61: 168–173, 2003.

[7] A. Cbers. Diffusion of magnetotactic bacterium in rotating magnetic field. *Journal of Magnetism and Magnetic Materials*, 323:279–282, 2011.

[8] J. Deseigne, S. Léonard, O. Dauchot, and H. Chaté. Vibrated polar disks: Spontaneous motion, binary collisions, and collective dynamics. *Soft Matter*, 8:5629–5639, 2012.

[9] W. R. DiLuzio, L. Turner, M. Mayer, P. Garstecki, D. B. Weibel, H. C. Berg, and G. M. Whitesides. Escherichia coli swim on the right-hand side. *Nature*, 435:1271–4, 2005.

[10] A. Einstein. Investigations on the Theory of Brownian Motion. *Ann. der Physik*, 1905.

[11] J. Elgeti, R. G. Winkler, and G. Gompper. Physics of microswimmers - Single particle motion and collective behavior: A review. *Reports on Progress in Physics*, 78, 2015.

[12] G. Frangipane, G. Vizsnyiczai, C. Maggi, R. Savo, A. Sciortino, S. Gigan, and R. Di Leonardo. Invariance properties of bacterial random walks in complex structures. *Nature Communications*, 2019.

[13] W. Gao and J. Wang. The environmental impact of micro/nanomachines: A review. *ACS Nano*, 8: 3170–3180, 2014.

[14] C. W. C. W. Gardiner and C. W. C. W. Gardiner. *Stochastic methods : a handbook for the natural and social sciences*. Springer, 2009.

[15] L. Hall-Stoodley, J. W. Costerton, and P. Stoodley. Bacterial biofilms: From the natural environment to infectious diseases, 2004.

[16] T. J. Higgins. Topics in the Theory of Random Noise, vol.1 (R. L. Stratonovich). *SIAM Review*, 1965.

[17] H. S. Jennings. On the Significance of the Spiral Swimming of Organisms. *The American Naturalist*, 1901.

[18] R. Kubo. Brownian motion and nonequilibrium statistical mechanics. *Science*, 233:330–334, 1986.

[19] S. Kudo, N. Imai, M. Nishitoba, S. Sugiyama, and Y. Magariyama. Asymmetric swimming pattern of Vibrio alginolyticus cells with single polar flagella. *FEMS Microbiology Letters*, 2005.

[20] F. Kümmel, B. ten Hagen, R. Wittkowski, D. Takagi, I. Buttinoni, R. Eichhorn, G. Volpe, H. Löwen, and C. Bechinger. Circular motion of asymmetric self-propelling particles Kümmel et al. Reply:. *Physical Review Letters*, 2014.

[21] E. Lauga and T. R. Powers. The hydrodynamics of swimming microorganisms. *Reports on Progress in Physics*, 72, 2009.

[22] E. Lauga, W. R. DiLuzio, G. M. Whitesides, and H. A. Stone. Swimming in circles: Motion of bacteria near solid boundaries. *Biophysical Journal*, 90:400–412, 2006.

[23] D. S. Lemons and A. Gythiel. Paul Langevin's 1908 paper "On the Theory of Brownian Motion" ["Sur la théorie du mouvement brownien," C. R. Acad. Sci. (Paris) 146 , 530–533 (1908)] . *American Journal of Physics*, 1997.

[24] G. Li, L. K. Tam, and J. X. Tang. Amplified effect of Brownian motion in bacterial near-surface swimming. *Proceedings of the National Academy of Sciences of the United States of America*, 2008.

[25] A. Morin, D. Lopes Cardozo, V. Chikkadi, and D. Bartolo. Diffusion, subdiffusion, and localization of active colloids in random post lattices. *Physical Review E*, 96:1–8, 2017.

[26] B. J. Nelson, I. K. Kaliakatsos, and J. J. Abbott. Microrobots for Minimally Invasive Medicine. *Annual Review of Biomedical Engineering*, 12:55–85, 2010.

[27] S. Palagi, A. G. Mark, S. Y. Reigh, K. Melde, T. Qiu, H. Zeng, C. Parmeggiani, D. Martella, A. Sanchez-Castillo, N. Kapernaum, F. Giesselmann, D. S. Wiersma, E. Lauga, and P. Fischer. Structured light enables biomimetic swimming and versatile locomotion of photoresponsive soft microrobots. *Nature Materials*, 15:647–653, 2016.

[28] J. Perrin. Mouvement brownien et réalité moléculaire. *Ann. Chim. Phys.*, 1909.

[29] K. E. Peyer, L. Zhang, and B. J. Nelson. Bio-inspired magnetic swimming microrobots for biomedical applications. *Nanoscale*, 5:1259–1272, 2013.

[30] R. Phillips and R. Milo. A feeling for the nnumbers in biology, 2009.

[31] W. C. Poon. From Clarkia to escherichia and janus: The physics of natural and synthetic active colloids. In *Proceedings of the International School of Physics "Enrico Fermi"*, 2012.

[32] S. Ramaswamy. The Mechanics and Statistics of Active Matter. *Annual Review of Condensed Matter Physics*, 2010.

[33] J. Schluter and K. R. Foster. The Evolution of Mutualism in Gut Microbiota Via Host Epithelial Selection. *PLoS Biology*, 10, 2012.

[34] J. E. Sosa-Hernández, M. Santillán, and J. Santana-Solano. Motility of Escherichia coli in a quasi-two-dimensional porous medium. *Physical Review E*, 95, 2017.

[35] S. Van Teeffelen and H. Löwen. Dynamics of a Brownian circle swimmer. *Physical Review E - Statistical, Nonlinear, and Soft Matter Physics*, 78, 2008.

[36] T. Vicsek and A. Zafeiris. Collective motion. *Physics Reports*, 517:71–140, 2012.

[37] G. Volpe and G. Volpe. The topography of the environment alters the optimal search strategy for active particles. *Proceedings of the National Academy of Sciences*, 114:11350–11355, 2017.

[38] M. von Smoluchowski. Zur kinetischen Theorie der Brownschen Molekularbewegung und der Suspensionen. *Annalen der Physik*, 326:756–780, 1906.

[39] E. W. Weisstein. "circle-circle intersection." from mathworld- - a wolfram web resource. http://mathworld.wolfram.com/circle-circleintersection.html.

[40] H. Wioland, F. G. Woodhouse, J. Dunkel, J. O. Kessler, and R. E. Goldstein. Confinement stabilizes a bacterial suspension into a spiral vortex. *Physical Review Letters*, 110, 2013.

[41] D. M. Woolley. Motility of spermatozoa at surfaces. *Reproduction*, 126:259–270, 2003.

Appendices

Appendix A

Useful integral

The calculation of the first and second moments of an active particle's position involves solving the integrals:

$$\langle \cos\phi \rangle = \int_{-\infty}^{+\infty} \cos\alpha\phi \frac{1}{\sqrt{2\sigma^2}} e^{\frac{-(\phi-\phi_0)^2}{2\sigma^2}} d\phi = \mathrm{Re}\Big[\int_{-\infty}^{+\infty} e^{i\alpha\phi} \frac{1}{\sqrt{2\sigma^2}} e^{\frac{-(\phi-\phi_0)^2}{2\sigma^2}} d\phi\Big]$$

$$\langle \sin\phi \rangle = \int_{-\infty}^{+\infty} \sin\alpha\phi \frac{1}{\sqrt{2\sigma^2}} e^{\frac{-(\phi-\phi_0)^2}{2\sigma^2}} d\phi = \mathrm{Im}\Big[\int_{-\infty}^{+\infty} e^{i\alpha\phi} \frac{1}{\sqrt{2\sigma^2}} e^{\frac{-(\phi-\phi_0)^2}{2\sigma^2}} d\phi\Big]$$

performing the change of variable $y = \phi - \phi_0$ we can rewrite this intergral as

$$e^{i\alpha\phi_0} \frac{1}{\sqrt{2\sigma^2}} \int_{-\infty}^{+\infty} e^{\frac{-(y^2 - i\alpha\phi_0 2\sigma^2)}{2\sigma^2}} dy =$$

(using now the substitution $k = y - i\alpha\sigma^2$)

$$= e^{i\alpha\phi_0} \frac{1}{\sqrt{2\sigma^2}} \int_{-\infty}^{+\infty} e^{\frac{-(k+i\alpha\sigma^2)(k-i\alpha\sigma^2)}{2\sigma^2}} dk = \Big[e^{i\alpha\phi_0} \frac{1}{\sqrt{2\sigma^2}} \int_{-\infty}^{+\infty} e^{\frac{-k^2}{2\sigma^2}} e^{\frac{\sigma^2}{2}} dk\Big] e^{\frac{-\alpha\sigma^2}{2}} =$$

$$= e^{i\alpha\phi_0 - \frac{\alpha\sigma^2}{w}}$$